G. Zamora-Caballero, R. Vazquez, F. Topputo
Solar Sail Trajectory Optimization for Asteroid Flyby and Rendezvous
Journal of Guidance Control and Dynamics, Vol. 48, N. 10, p. 2257-2271, 2025 (published online 02/06/2025)
doi:10.2514/1.g008632

Solar Sail Trajectory Optimization for Asteroid Flyby and Rendezvous

Gonzalo Zamora-Caballero*, Rafael Vazquez†
University of Seville, Higher Technical School of Engineering
Camino de los Descubrimientos s.n 41092 Sevilla, Spain

Francesco Topputo‡
Polytechnic University of Milan, Via La Masa 34, 20156 Milano, Italy

Solar System exploration has emerged as a primary focus in the space community, with deep-space CubeSats standing out as a promising solution for studying asteroids within the Solar System. This paper specifically addresses missions employing solar sail technology, aiming to explore the attainable reachability of a miniaturized solar sail departing from Earth. This is achieved by considering both flyby and rendezvous missions. Drawing inspiration from previous research using low-thrust propulsion, this work focuses on time-optimal missions, applying optimal control theory to achieve reasonable transfer times. The formulation relies on continuous guidance control, employing an indirect method derived from Euler-Lagrange variational equations and Pontryagin's Minimum Principle. Results show that the algorithm is a versatile tool obtaining optimal solutions for missions involving trajectories with multiple flybys.

Nomenclature

A	=	Linear dynamics matrix
$\mathbf{a}_n$	=	Solar sail normal acceleration
c	=	Speed of light
H	=	Hamiltonian
$H_{\alpha,\alpha}$, $H_{\alpha,\delta}$	=	Hessian submatrices
$\mathbf{I}$	=	Identity matrix
I	=	Solar irradiance
$\hat{\mathbf{i}}_h$	=	Heliocentric angular momentum unit vector
$\hat{\mathbf{i}}_r$	=	Sunlight unit vector

*MSc graduate, Aerospace Engineering Department, gonzalozamorac@gmail.com, AIAA Student Member
†Professor, Aerospace Engineering Department, rvazquez1@us.es
‡Professor, Department of Aerospace Science and Technology, francesco.topputo@polimi.it, AIAA Senior Member

$\hat{\mathbf{i}}_\theta$ = Unit vector to complete the reference frame

J = Time-optimal objective functional

$\mathcal{J}$ = Jacobian matrix

l = Time-optimal cost function

m = Number of interior point constraints

$\mathbf{n}$ = Solar sail normal unitary vector

N_h = Number of points of the mission grid

p = Number of intermediate flybys

P = Solar sail pressure

$\mathbf{P}$ = Lagrange polynomial interpolator

n = Number of interpolation points

$\mathbf{r}$ = Position vector

t = Time

U = Set of admissible controls

$\mathbf{u}$ = Control vector

$\mathbf{v}$ = Velocity vector

$\mathbf{x}$ = State

α = Solar sail cone angle

β = Solar sail lightness number

δ = Solar sail clock angle

μ = Sun gravitational parameter

Φ = State transition matrix

Ψ = Asteroid ephemeris

$\boldsymbol{\lambda}$ = Lagrange multipliers or costate variables

$\boldsymbol{\pi}$ = Interior constraint associated costate vector

σ = Solar sail areal density

Subscripts

a = Asteroid

fb = Flyby asteroid

I. Introduction

Deep-space CubeSats offer the potential to enhance and diversify Solar System exploration, as highlighted by [1]. More specifically, they hold promise for the exploration and characterization of the population of asteroids in orbit around the Solar System. The small size and low cost of deep-space CubeSats make them particularly well-suited for asteroid exploration, as they can be deployed in larger numbers and provide a cost-effective means of studying these celestial bodies. Deep-space CubeSats are part of recent missions, including Juventas [2] and LICIACube [3]. Another example is Milani [4], a 6U CubeSat that will be released in the Didymos binary asteroid system by ESA's Hera spacecraft, with the objectives of studying and characterizing the system's asteroids. This recent trend demonstrates that deep-space CubeSats present a lower-cost exploration alternative compared to traditional spacecraft, offering high science-to-investment ratios [1, 5].

Solar sailing is an emerging and promising technology that offers the potential for longer-duration missions, higher velocity increments [6], and significant launch window flexibility [7] compared to conventional chemical or electric propulsion. Solar sailing utilizes large-area reflective films to harness solar radiation pressure (solar photons) for spacecraft propulsion [6]; see [8] for a comprehensive overview of solar sail technology. The use of solar sailing in deep-space CubeSat missions has the potential to extend mission durations and enable the exploration of a wider range of asteroid targets, as the propulsion system does not rely on a finite supply of fuel. Although solar sails have attracted considerable interest since the early 1990s, a pivotal milestone was reached in May 2010 with the launch of IKAROS (Interplanetary Kite-craft Accelerated by Radiation Of the Sun) by JAXA (Japanese Aerospace Exploration Agency) [9]. The success of IKAROS and other demonstrations, such as Lightsail-1 [10] and Lightsail-2 [11] by the Planetary Society, DeorbitSail [12] by the European Commission, Cubesail [13] by ESA, Sunjammer [14] by NASA, and InflateSail [15] by the University of Surrey, have proven the effectiveness and potential of solar sailing for interplanetary travel [16, 17].

As a result, various space agencies are actively planning or proposing multiple solar sail-based space exploration missions to explore and study different asteroids [4]. One of the most notable examples, which serves as a reference model throughout this article, is NASA's NEA (near-Earth asteroid) Scout mission. NEA Scout employs an 86 m^2 solar sail deployed from a 6U CubeSat [18]. In addition to NEA Scout, numerous missions have been proposed in this decade, including NASA's Solar Cruiser for heliophysics [19] and JAXA's OKEANOS for Jupiter Trojan asteroid exploration [20].

While past studies have explored asteroid accessibility using low-thrust electric propulsion [1], there remains room for further investigation into the analysis of minimum-time missions of asteroids using miniaturized solar sails. This paper contributes to this area of research by examining the optimal trajectory design for a solar sail, using the NEA Scout mission as a case study. Our objectives are to develop an indirect optimization framework to analyze the reachability of asteroids using a miniaturized solar sail, considering both flyby and rendezvous scenarios, and to assess the range of potential target asteroids accessible to such a probe within practical transfer times.

[21]

The main contributions of this paper, compared to existing works in the literature, are: 1) The development of a method to address single or multi-body visitation missions using solely an indirect approach formulation, with a detailed derivation of the control law and necessary conditions for optimality, particularly in the case of control saturation, 2) the introduction of an analytical formulation of the problem's Jacobian matrix, to mitigate the dependence on initial guess parameters and improve the convergence capabilities of the method, and 3) the development of an algorithm capable of conducting a minimum-time mission analysis from Earth to NEA targets using solar sail-based propulsion, extending the results of [1], which focused on low-thrust electric propulsion. The algorithm can handle both single and multiple asteroid visitation missions.

This article considers the ideal reflection assumption of solar radiation pressure (SRP), which has been adopted in several studies [22]. This is a simple mathematical model of an geometrically ideal sail. McInnes [8] develops the solar force taking into account the reflectance, absorption and emissivity of the solar sail. Some works as [23] find time-optimal solar-sail trajectories making use of the so-called optical force model it is possible to express the total force exerted due to the solar radiation pressure on the solar sail. These sail optical parameters are function of the sail geometry. In [21] it is defined the methodology for the analytic description of the force and moment generated by a solar sail of arbitrary shape and surface optical properties. Additionally, a classical assumption is made regarding the possible attitude constraints with respect to the solar sail. While this assumption simplifies the analysis, it is important to acknowledge that attitude operational limits play a critical role in the feasibility of solar sail missions, particularly in terms of power generation and thermal control [24].

Several specific studies have served as reference points for this work, and their results are reproduced to validate the model. For instance, [23] employs a non-ideal solar sail model and calculates time-optimal trajectories using a specific implementation of a direct pseudo-spectral method, with initial guesses generated via a genetic algorithm. [25] investigates both ideal and non-ideal scenarios utilizing an indirect approach for three-dimensional problems encompassing elliptical and non-coplanar orbits. [26] and [22] adopt an indirect optimization approach and address the issue of incorporating sail attitude constraints with an ideal reflection SRP, alongside practical mission considerations. [27], [28], and [6] present a comprehensive perspective, utilizing a non-ideal model, with a detailed development of the indirect approach and mathematical optimization of the problem. These works provide a unified framework for optimizing solar-sailing trajectories while incorporating practical mission considerations, including imperfect SRP reflection and sail attitude constraints, in a coordinate-independent manner. Furthermore, while the majority of the aforementioned studies concentrate on single-target missions, some works have also addressed the multi-target rendezvous problem for solar sails. Among these are the work of [29], which makes use of a sequence search by means of a simplified trajectory model and a set of heuristic rules plus a subsequent optimization phase, and [30], which employs a numerical method combining a global optimization algorithm and a nonlinear equation solver to obtain the

optimal solution.

This paper is organized as follows. Section II provides a brief introduction to the models used for orbital motion and solar sail thrust. Optimal control theory applied to the derivation of time-optimal trajectories is developed in Section III. Following that, Section IV addresses the practical implementation, elucidating the algorithm developed and its efficacy in resolving the significant dependence on the initial guess. Finally, conclusions are drawn from the results obtained in Section V.

II. Assumptions and problem statement

The goal of the paper is the analysis of the envelope of asteroids that can be accessed by a miniaturized solar sail within a reasonable transfer timeframe. Consequently, the most basic scenario is a single rendezvous problem with an arbitrary asteroid, departing from the Earth. Hence, this involves the selection of both an astrodynamics model and a solar sail propulsion model, which are outlined in Section II.A. Following this, Section II.B formulates the problem of finding time-minimal trajectories.

A. Mission assumptions

In terms of astrodynamics modeling, the work is framed within the two-body problem (TBP). Given the low mass of the majority of asteroids and their negligible influence on the spacecraft motion, the TBP serves as the most intuitive and straightforward model, offering a sufficiently accurate representation.

For the interplanetary transfer trajectory in deep space, the ideal solar sail is considered under the following assumptions [31]: 1) Solar sail is assumed as a flat plate; 2) Solar gravitation and solar radiation pressure are the only forces acting on the sail, there are no other perturbation forces; 3) The attitude of the solar sail can be changed instantaneously.

This model represents a geometrically ideal solar sail. The purpose of these assumptions is to simplify the force analysis, reduce the design to a single parameter, and exclude the need for an attitude control system. The simplified geometry reduces the complexity of the sail's dynamics. This mathematical abstraction deviates significantly from real-world scenarios, where numerous perturbative forces are present. In this article, it is demonstrated that such perturbations, although negligible, can be readily incorporated into the model without altering the optimization framework. The solution obtained for the ideal case can be adopted as an initial guess for solving the non-ideal case, a development which is left for future work. This simplified model serves as a guide in the design of the initial stages of mission planning, whereas, in more complex implementations, the aforementioned factors influence the solar sail's performance.

The solar sail is characterized by its unit vector, $\mathbf{n}$. This normal vector is represented using a local rotating reference frame in Figure 1. Construction of this local frame utilizes the sunlight vector ($\hat{\mathbf{i}}_r$), the unit vector representing

heliocentric angular momentum ($\hat{\mathbf{i}}_h$), and a third vector that completes the right-hand system ($\hat{\mathbf{i}}_\theta$).

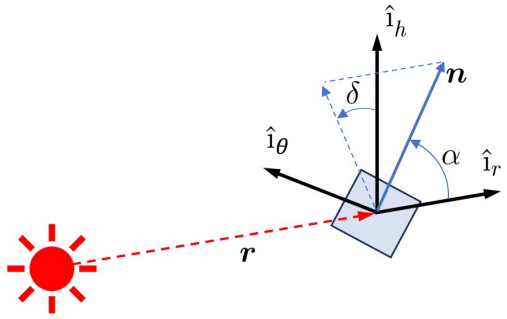

Fig. 1 Rotating frame and sail attitude representation with normal vector.

The parameterization of this vector involves two attitude angles: 1) the cone angle $\alpha \in [0,\ \pi/2]$, and 2) the clock angle $\delta \in [-\pi,\ \pi]$.

It is crucial to emphasize that these two angles are subject to constraints due to the inherent limitation of the solar sail in generating an acceleration component directed toward the Sun; the normal vector consistently orients away from the Sun.

This framework yields the following definition of the normal vector with respect to the frame:

$$\mathbf{n}_{\hat{\mathbf{i}}_r,\hat{\mathbf{i}}_\theta,\hat{\mathbf{i}}_h} = \begin{bmatrix} \cos\alpha \\ \sin\alpha\sin\delta \\ \sin\alpha\cos\delta \end{bmatrix} \tag{1}$$

Concerning the modeling of sail propulsion, a simplified model for the sail is developed, selecting an ideal solar sail (perfectly reflective) model. Under this assumption, only an acceleration component perpendicular to the sail is considered [8]. Hence, the influence of the solar sail (total force considering the ideal sail scenario) can be represented by determining the magnitude of the acceleration component in the direction normal to the surface.

Given the mass per unit area σ (areal density), the acceleration per unit area is $a = 2I/c\sigma$. Here, I represents the constant solar intensity or irradiance, and c denotes the speed of light. The solar radiation pressure exerted over the surface, assuming a perfectly reflective model, equals $2I/c$ [8].

Therefore, the definition of the acceleration vector is modelled as follows:

$$\mathbf{a_n} = \frac{2I}{c\,\sigma}\cos^2\alpha\,\mathbf{n} \tag{2}$$

This acceleration is expressed as a fraction of the local acceleration due to the Sun's Two-Body Problem, exerted acceleration μ/r^2.

$$\mathbf{a_n} = \frac{\mu\beta}{r^4}(\mathbf{r}\cdot\mathbf{n})^2\,\mathbf{n} = \frac{\mu\beta}{r^2}(\cos\alpha)^2\,\mathbf{n} \tag{3}$$

being $\mathbf{r}$ the relative position between the Sun and the spacecraft in the TBP. β is the *lightness number of the sail*, which describes the acceleration capability of the sail. It represents the dimensionless ratio of the maximum vehicle acceleration divided by the Sun's local gravity $g = \mu/r^2$, where $\mu = GM_S$ and M_s denotes the mass of the Sun:

$$\beta = \frac{\frac{2I}{c\,\sigma}}{\mu/r^2} \tag{4}$$

It is important to note that the lightness number is also independent of distance from the Sun. This independence arises because both gravity and solar radiation pressure decrease as the inverse square of the distance from the Sun. As a result, this number determines the feasibility of any given orbit maneuvers for a solar sail [32].

Limitations in the cone angle are introduced to simulate a more realistic behavior:

$$\alpha_{min} \leq \alpha \leq \alpha_{max} \tag{5}$$

Indeed, these constraints are justified by the imposition of maximum and minimum limits to ensure sufficient power generation and thermal control of the vehicle, respectively [6]. A large cone angle may reduce the efficiency of the solar radiation pressure force, necessitating the upper bound [33]. Conversely, the lower bound ensures that the vehicle maintains adequate thermal control. For example, in engineering practices such as the NEA Scout mission, a maximum solar angle constraint of $\alpha_{\max} = 40 - 50\,\text{deg}$ must be enforced according to [6]. In the model employed in this paper, a minimum cone angle value of $\alpha_{\min} = 0\,\text{deg}$ is maintained.

Furthermore, the asteroids ephemeris are considered to describe their motion. Employing an interpolation method inspired by [34], the ephemeris are interpolated to generate the position and velocity of the target asteroid whenever necessary.

Given the data of an asteroid, if the position and velocity at an epoch t are to be computed, n points close to it are employed: $(\mathbf{r}_1(t_1), \mathbf{v}_1(t_1)), (\mathbf{r}_2(t_2), \mathbf{v}_2(t_2)), \ldots, (\mathbf{r}_n(t_n), \mathbf{v}_n(t_n))$. The Lagrange interpolating polynomial* is the polynomial of degree $\leq (n-1)$ that passes through these n points.

$$\begin{bmatrix}\mathbf{r}(t)\\ \mathbf{v}(t)\end{bmatrix} = \sum_{j=1}^{n}\begin{bmatrix}\mathbf{r}(t_j)\\ \mathbf{v}(t_j)\end{bmatrix}\prod_{k=1,k\neq j}^{n}\frac{t-t_k}{t_j-t_k} \tag{6}$$

Therefore, a sliding Lagrange polynomial method (commonly used in GPS systems) is developed from the real data

*`https://mathworld.wolfram.com/LagrangeInterpolatingPolynomial.html` (last visited on 15/05/2024)

obtained from the *Horizons Web Application*[†]. As well as NASA's SPICE[‡] kernels to describe the motion of the planets.

B. Statement of the problem

With the assumptions above and, assuming the Sun centered at the Solar System barycenter (SSB), the equations of motion are:

$$\dot{\mathbf{x}} = \mathbf{f}(\mathbf{x}, \mathbf{u}, t) \quad \begin{cases} \dot{\mathbf{r}} = \mathbf{v} \\ \dot{\mathbf{v}} = -\mu_S \dfrac{\mathbf{r}}{r^3} + \dfrac{\mu\beta}{r^2}(\cos\alpha)^2\,\mathbf{n} \end{cases} \tag{7}$$

where $\mathbf{x} := (\mathbf{r},\ \mathbf{v})$ is the state made of position and velocity, respectively, $\mathbf{f}$ is the vector field and μ is the standard gravitational parameter of the Sun. $\mathbf{u}(t)$ is the control law vector and the set of admissible controls is

$$\mathbf{u} := [\alpha,\ \delta]^T \in U \quad U := \{(\alpha, \delta) :\ \alpha \in [0, \alpha_{max}],\ \delta \in [-\pi, \pi]\} \tag{8}$$

where α_{max} can be as large as 90 deg.

The initial state value $\mathbf{x}_0$ is determined by the ephemeris of the Earth on the day of launch. Additionally, the final condition must adhere to a terminal constraint, which is precisely defined as:

$$\mathbf{x}(t_f) = \boldsymbol{\Psi}(t_f) = \begin{bmatrix} \mathbf{r}_a(t_f) \\ \mathbf{v}_a(t_f) \end{bmatrix} \tag{9}$$

the ephemeris of the asteroid at final time t_f: position $\mathbf{r}_a(t_f)$ and velocity $\mathbf{v}_a(t_f)$.

The problem belongs to the continuous guidance domain where the control action, in this case the solar sail normal vector, is applied continuously over finite time intervals. By controlling this normal vector, the orientation of the sail relative to the Sun is altered, resulting in the gain or loss of orbital angular momentum [8].

The statement of the bounded continuous control problem, for a solar sail transfer and a time-optimal solution, can be formulated as [35]:

$$\min_{\mathbf{u}\in U} \quad J := \int_{t_0}^{t_f} 1\,\mathrm{d}t \quad st. \begin{cases} \dot{\mathbf{x}} = \mathbf{f}(\mathbf{x}, \mathbf{u}, t) \\ \mathbf{x}(t_0) = \mathbf{x}_0 \\ \mathbf{x}(t_f) = \boldsymbol{\Psi}(t_f) \end{cases} \tag{10}$$

where J is the objective functional.

[†] `https://ssd.jpl.nasa.gov/horizons/app.html#/` (last visited on 01/06/2024)

[‡] `https://naif.jpl.nasa.gov/naif/spiceconcept.html` last visited on (01/06/2024)

III. Methodology

Section III elucidates and formulates the application of optimal control theory to the derivation of time-optimal trajectories. The necessary conditions for a time-optimal asteroid interception problem are established in Section III.A, while Section III.B develops the optimal control law. Additionally, the formulation for a mission involving multiple bodies is addressed in Section III.C.

A. Optimal solar sailing transfer problem

Defining the Hamiltonian [35] of the system from the cost ($l(t, \mathbf{x}, \mathbf{u}) = 1$) and the dynamics such that

$$H(t, \mathbf{x}, \mathbf{u}, \boldsymbol{\lambda}) = l(t, \mathbf{x}, \mathbf{u}) + \boldsymbol{\lambda}^T \mathbf{f}(\mathbf{x}, \mathbf{u}, t) = 1 + \boldsymbol{\lambda}_r \cdot \mathbf{v} - \mu \frac{\mathbf{r} \cdot \boldsymbol{\lambda}_v}{r^3} + \boldsymbol{\lambda}_v \cdot \frac{\mu\beta}{r^4} (\mathbf{r} \cdot \mathbf{n})^2 \mathbf{n} \tag{11}$$

where $\boldsymbol{\lambda} = [\boldsymbol{\lambda}_r,\ \boldsymbol{\lambda}_v]^T \in \mathbb{R}^{6x1}$ is the vector *Lagrange multipliers* or *costate variables*. The Euler–Lagrange differential-algebraic equations (DAEs) are stated as

$$\begin{aligned}
&\dot{\mathbf{x}} = \frac{\partial H}{\partial \boldsymbol{\lambda}} \quad \mathbf{x}(t_0) = \mathbf{x}_0 \quad \mathbf{x}(t_f) = \boldsymbol{\Psi}(t_f) \\
&\dot{\boldsymbol{\lambda}} = -\frac{\partial H}{\partial \mathbf{x}} \\
&0 = \frac{\partial H}{\partial \mathbf{u}} \\
&0 = H(t_f) - \boldsymbol{\lambda}(t_f)^T \dot{\boldsymbol{\Psi}}(t_f)
\end{aligned} \tag{12}$$

This system of DAEs is completed adding the necessary conditions for a free final time with a rendezvous terminal constraint, given by a scalar condition, denoted as transversality condition.

Taking into account the analytical results from solar sail propulsion and applying the Euler–Lagrange costate dynamic differential equation:

$$\begin{aligned}
\dot{\mathbf{x}} &= \mathbf{f}(\mathbf{x}, \mathbf{u}, t) \\
\dot{\boldsymbol{\lambda}}_r &= -\left(3\frac{\mu}{r^5}\mathbf{r}\,\mathbf{r}^T - \frac{\mu}{r^3}\mathbf{I}_{3x3}\right)\boldsymbol{\lambda}_v - 2\frac{\beta\mu}{r^4}(\mathbf{r}\cdot\mathbf{n})(\mathbf{n}\cdot\boldsymbol{\lambda}_v)\left[\mathbf{n} - \frac{2(\mathbf{r}\cdot\mathbf{n})\,\mathbf{r}}{r^2}\right] \\
&\quad - \frac{\beta\mu}{r^4}\left[\frac{\partial \mathbf{n}}{\partial \mathbf{r}}\right]^T (\mathbf{r}\cdot\mathbf{n})\,(2(\mathbf{n}\cdot\boldsymbol{\lambda}_v)\,\mathbf{r} + (\mathbf{r}\cdot\mathbf{n})\,\boldsymbol{\lambda}_v) \\
\dot{\boldsymbol{\lambda}}_v &= -\boldsymbol{\lambda}_r - \frac{\beta\mu}{r^4}\left[\frac{\partial \mathbf{n}}{\partial \mathbf{v}}\right]^T (\mathbf{r}\cdot\mathbf{n})\,(2(\mathbf{n}\cdot\boldsymbol{\lambda}_v)\,\mathbf{r} + (\mathbf{r}\cdot\mathbf{n})\boldsymbol{\lambda}_v)
\end{aligned} \tag{13}$$

which stands for a system of 12 dimensional ordinary differential equations (ODEs).

Note that, in the position and velocity costate differential equations in 13, there is an additional term:

$$\frac{\beta\mu}{r^4}\left[\frac{\partial \mathbf{n}}{\partial \mathbf{x}}\right]^T (\mathbf{r}\cdot\mathbf{n})\,(2(\mathbf{n}\cdot\boldsymbol{\lambda}_v)\,\mathbf{r} + (\mathbf{r}\cdot\mathbf{n})\boldsymbol{\lambda}_v) \tag{14}$$

This concerns the dependency of the defined normal vector on the radial and velocity directions. To the best of the author's knowledge, this term is not included in any paper. In the bibliography, references such as [22], [25], and [36] do not appear to explicitly consider these terms. Indeed, when applying the optimal control law (Equation 24), these terms vanish from the Euler-Lagrange costate differential equations (13), as will be demonstrated subsequently (Equation 30).

However, ensuring the correct integration of these differential equations is essential. These expressions become particularly significant when any of the control input variables reach saturation, as it is discussed in Section III.B. Notably, saturation is not applied to the clock angle, allowing the derivatives to be simplified using the optimal control law (Equation 22). Nonetheless, saturation in the cone parameter angle is a common constraint in this solar sail transfer, as detailed in the Mission Assumptions (Equation 5). Consequently, the optimal control law (Equation 23) associated with this control angle cannot be applied due to this restriction.

Concerning equation 10, fixed conditions for all states are specified at the initial and terminal constraints. Therefore, following the Euler–Lagrange necessary conditions, no constraint is imposed on these costates. The integration of the system of DAEs (Equation 13) needs to satisfy the final constraints of the two-point boundary value problem (TPBVP):

$$\mathbf{r}_a(t_f) - \mathbf{r}(t_f) = 0 \tag{15a}$$

$$\mathbf{v}_a(t_f) - \mathbf{v}(t_f) = 0 \tag{15b}$$

$$H(t_f) - \boldsymbol{\lambda}(t_f)^T \dot{\boldsymbol{\Psi}}(t_f) = H(t_f) - \boldsymbol{\lambda}_r^T(t_f)\,\mathbf{v}_a(t_f) - \boldsymbol{\lambda}_v^T(t_f)\left(-\frac{\mu}{||\mathbf{r}_a(t_f)||^3}\mathbf{r}_a(t_f)\right) = 0 \tag{15c}$$

B. Optimal control law

The Pontryagin's Minimum Principle [37] states that: being $(\mathbf{x}^*, \mathbf{u}^*)$ an optimal process of the above singular control problem, there exists a 6-dimensional vector function $\boldsymbol{\lambda}$ which verifies the condition of non-triviality ($\boldsymbol{\lambda}(t) \neq 0$ for all $t \in [t_0, t_f]$), the states and the costates dynamics (12), the transversality condition (15c), and the Hamiltonian minimizing condition:

$$\mathbf{u}^* = \underset{\mathbf{u}\in U}{arg\ min}\, H(\mathbf{x}, \boldsymbol{\lambda}, \mathbf{u}) \tag{16}$$

The optimal control law differs from that corresponding to electrical low-thrust propulsion. In the latter scenario, the minimal Hamiltonian requires aligning the direction of low-thrust opposite to the velocity Lagrange multiplier $\boldsymbol{\lambda}_v$ [38]. However, this approach is not applicable in the case of solar sails due to the inability to continuously align the solar radiation pressure force along a specific vector, as it cannot consistently point sunward. Moreover, the magnitude of the solar radiation pressure force depends on the direction it forms with sunlight, as indicated in Equation 3.

Minimizing the Hamiltonian function entails the adjustment of the sail's attitude to minimize (11). Given that the control inputs parameterize the solar sail normal vector, the following expression illustrates the Hamiltonian's reliance on the control vector:

$$\mathbf{u}^*(\alpha^*, \delta^*) = \underset{\mathbf{u}\in U}{arg\ min}\, (\mathbf{r}\cdot\mathbf{n})^2 \boldsymbol{\lambda}_v \cdot \mathbf{n} \tag{17}$$

As a general nonlinear function takes its minimum at either a local minimum within its domain (which corresponds to the Euler–Lagrange condition) or at one of the domain's endpoints, the equation presents two categories of candidate solutions: local minimum solutions within the domain, and boundary solutions. Hence, it would be necessary to examine these boundary conditions as well.

Therefore, a classical quadratic optimization problem is set where the optimal control vector $\mathbf{u}^* = (\alpha^*, \delta^*)$ has to verify

$$\frac{\partial H}{\partial \mathbf{u}}(t, \mathbf{x}^*(t), \mathbf{u}^*(t), \boldsymbol{\lambda}(t)) = \mathbf{0}, \quad \frac{\partial^2 H}{\partial \mathbf{u}^2}(t, \mathbf{x}^*(t), \mathbf{u}^*(t), \boldsymbol{\lambda}(t)) \geq 0 \quad \forall t \in [t_0, t_f] \tag{18}$$

Describing the orientation of the velocity costate vector in the local rotating frame

$$\boldsymbol{\lambda}_v = \lambda_v \hat{\boldsymbol{\lambda}}_v = \lambda_v \left(\cos\tilde{\alpha}\,\hat{\mathbf{i}}_r + \sin\tilde{\alpha}\sin\tilde{\delta}\,\hat{\boldsymbol{\theta}} + \sin\tilde{\alpha}\cos\tilde{\delta}\,\hat{\mathbf{h}}\right) = [\lambda_{v_x}\ \lambda_{v_y}\ \lambda_{v_z}]^T \tag{19}$$

where $\tilde{\alpha} \in [0, \pi]$ is the angle formed by the primer vector and the sunlight:

$$\tilde{\alpha} = \arccos\left(\frac{\mathbf{r}}{r}\cdot\frac{\boldsymbol{\lambda_v}}{\lambda_v}\right) \in [0, \pi] \tag{20}$$

and $\tilde{\delta} \in [0, 2\pi]$ determines the azimuthal angle in a plane normal to $\mathbf{r}$:

$$\tilde{\delta} = \text{atan2}\left(\frac{\hat{\boldsymbol{\lambda}}_v \cdot \hat{\boldsymbol{\theta}}}{\hat{\boldsymbol{\lambda}}_v \cdot \hat{\mathbf{h}}}\right) \in [0, 2\pi] \tag{21}$$

similarly to the definition of the control normal vector with respect to the local frame in 1.

Applying Legendre-Clebsch conditions (18) yields to

$$\delta^* = \text{arctan2}\left(-\lambda_{v_y}, -\lambda_{v_z}\right) = \pi + \tilde{\delta} \tag{22}$$

which implies that the normal vector (control vector) lies in the plane defined by the sunlight and $\boldsymbol{\lambda}_v$ (Figure 2).

The solution of the second order equation $H_\alpha = 0$ leads to

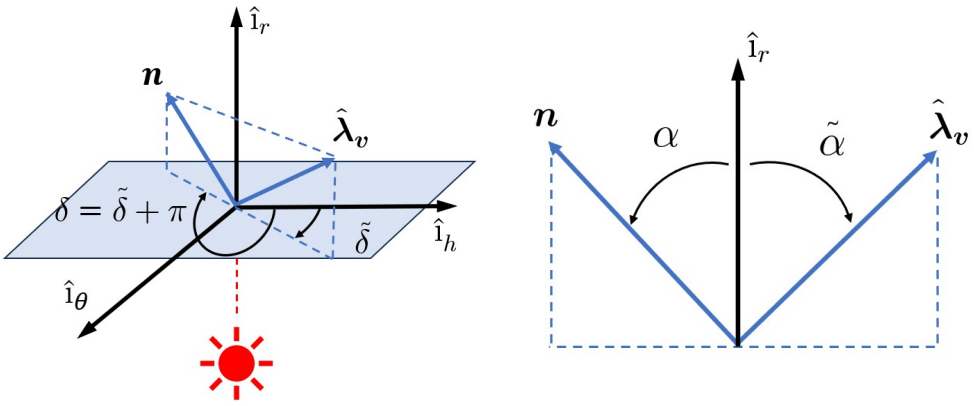

Fig. 2 Normal vector and the velocity costate vector.

$$\tan\alpha^\star = \frac{3}{4}\tan\left(\pi/2 - \tilde{\alpha}\right) \pm \frac{1}{4}\sqrt{9\left(\tan\left(\pi/2 - \tilde{\alpha}\right)\right)^2 + 8} \tag{23}$$

Applying the generalized Legendre-Clebsch condition to be accomplished for a minimum, the sign must be selected so that the positive definiteness of the Hessian is achieved. Since, if $\delta = \delta^*$, $H_{\alpha\delta} = 0$, therefore, in order to guarantee the positive-definiteness of the Hessian matrix, then $H_{\alpha\alpha} \geq 0$. This leads to the conclusion that, regardless of the $\tilde{\alpha}$ value, the positive sign in (23) is required to satisfy this condition, which is corroborated by [27].

In Figure 3, the Hamiltonian function dependency with angle α is represented for different values of $\tilde{\alpha}$. As it can be observed, in case the cone angle is bounded as $\alpha \in [0,\ \pi/2]$, $\alpha^\star$ (solution with + sign) is always inside the domain [27]. The solution of Equation 23 with negative sign stands for the maximum of each curve. The numerical implications of incorporating constraints on α within the range $\alpha \in [0,\ \alpha_{\max}]$, suggest that the optimal solution is the constraint which is closest to $\alpha^\star$. The saturated $\alpha = \alpha_{max}$ is the value that minimises the Hamiltonian. Figure 3 visually demonstrates the effect of these constraints.

Thus, the solution for the ideal reflection model with restricted cone angle is the following one (24).

$$\mathbf{u}^* = [\alpha^* \quad \delta^*]^T \in U, \qquad \begin{cases} \alpha^* = \underset{\alpha\in\{\alpha_{min},\alpha^\star,\alpha_{max}\}}{arg\ min} \quad H(\alpha) \\ \delta^* = \arctan2(-\lambda_{v_y}, -\lambda_{v_z}) \end{cases} \tag{24}$$

In the case of a non-ideal model, determining the optimal control law requires an approximation based on a first-order Taylor series expansion around the value obtained for the ideal case [6]. For the ideal case, under the stated assumptions, the computed optimal value is exact and achievable under the perfect solar radiation pressure assumption. The value obtained in the ideal sail scenario can serve as an initial estimate for a nonlinear system solver, which determines the optimal control parameters. However, this development falls outside the scope of the present manuscript.

Once the necessary conditions for optimality have been developed and the analytical results from solar sail propulsion

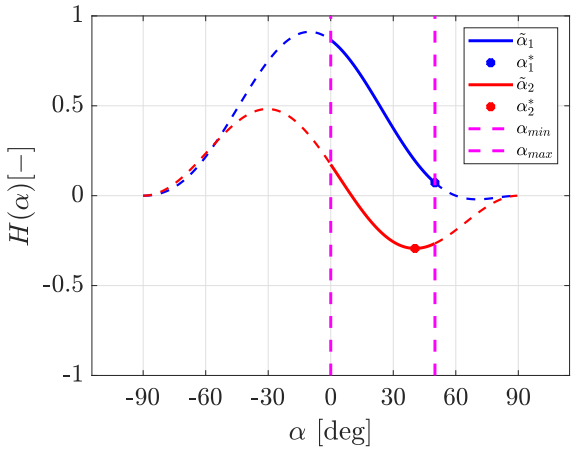

Fig. 3 Hamiltonian dependency on α with a maximum cone angle constraint.

have been considered, along with the application of the costate dynamic differential equation, the TPBVP is stated: find the unknowns $(\boldsymbol{\lambda}_0, t_f)$ so that, when integrating the state and costate dynamical model (13) with initial condition $\mathbf{x}_0$, verify the terminal condition Equation 15.

It is crucial to emphasize that the control input vector $\mathbf{u} := [\alpha, \delta]^T \in U$ determines the solar sail normal vector $\mathbf{n}$. Referring to Equation 1, this vector is defined in the International Celestial Reference Frame (ICRF) as

$$\mathbf{n} = \cos\alpha\,\hat{\mathbf{i}}_r + \sin\alpha\sin\delta\,\hat{\mathbf{i}}_\theta + \sin\alpha\cos\delta\,\hat{\mathbf{i}}_h \tag{25}$$

where $\hat{\mathbf{i}}_r$, $\hat{\mathbf{i}}_\theta$, and $\hat{\mathbf{i}}_h$ are the local rotating frame basis vectors expressed in the ICRF. This expression explicitly depends on both the sunlight direction $\mathbf{r}$ and the velocity vector $\mathbf{v}$, justifying the dependences of the normal vector appearing in 13. These expressions gain particular significance when any of the control input variables are saturated. As previously elucidated, saturation is not applied to the clock angle. Conversely, the event of saturation occurring in the cone parameter angle is considered and this dependency alters the Euler–Lagrange differential equation and even if it may have little influence on the computation of the minimum time to reach the asteroid, it does modify the system of ODEs. In the bibliography, references do not seem to consider these terms, at least explicitly. Indeed, when applying the optimal control law (24) and only in the non-saturation case, these terms vanish from the Euler–Lagrange costate differential equations (13), as will be demonstrated subsequently.

Firstly, it is intriguing to express the control vector $\mathbf{n}$ in terms of the cone angle α and the angle between the velocity costate and the sunlight $\tilde{\alpha}$. Given that the clock angle δ remains unconstrained, by applying $\delta^* = \tilde{\delta} + \pi$ [33],

$$\mathbf{n}(\alpha, \delta^*) = \cos\alpha\,\hat{\mathbf{i}}_r - \frac{\sin\alpha}{\sin\tilde{\alpha}}\left(\frac{\boldsymbol{\lambda}_v}{\lambda_v} - \cos\tilde{\alpha}\,\hat{\mathbf{i}}_r\right) = \frac{\sin(\alpha+\tilde{\alpha})}{\sin\tilde{\alpha}}\frac{\mathbf{r}}{r} - \frac{\sin\alpha}{\sin\tilde{\alpha}}\frac{\boldsymbol{\lambda}_v}{\lambda_v} \tag{26}$$

This applicability persists as δ^* is solely dependent on the velocity costate vector, rendering it independent of the

state variables. This observation confirms that

$$\left[\frac{\partial \mathbf{n}(\alpha,\delta)}{\partial \mathbf{x}}\right]_{\delta=\delta^*} = \left[\frac{\partial \mathbf{n}(\alpha,\delta^*)}{\partial \mathbf{x}}\right] \tag{27}$$

Hence, the derivatives that have not been explicitly stated in 13 can be replaced by

$$\begin{cases} \dfrac{\partial \mathbf{n}}{\partial \mathbf{r}} = \dfrac{\sin(\alpha+\tilde{\alpha})}{\sin\tilde{\alpha}}\left(\dfrac{\mathbf{I}_{3x3}}{r} - \dfrac{\mathbf{r}\mathbf{r}^T}{r^3}\right) - \dfrac{\sin\alpha}{\sin(\tilde{\alpha})^2}\left[\dfrac{\partial\tilde{\alpha}}{\partial\mathbf{r}}\right]^T\dfrac{\mathbf{r}}{r} + \dfrac{\cos\tilde{\alpha}\sin\alpha}{\sin(\tilde{\alpha})^2}\left[\dfrac{\partial\tilde{\alpha}}{\partial\mathbf{r}}\right]^T\dfrac{\boldsymbol{\lambda}_v}{\lambda_v} \\ \dfrac{\partial \mathbf{n}}{\partial \mathbf{v}} = \mathbf{0}_{3x3} \end{cases} \tag{28}$$

where

$$\frac{\partial\tilde{\alpha}}{\partial\mathbf{r}} = \frac{1}{\sin\tilde{\alpha}}\left[\frac{\mathbf{r}^T\boldsymbol{\lambda}_v}{\lambda_v\, r^3}\mathbf{r} - \frac{\boldsymbol{\lambda}_v}{\lambda_v\, r}\right] \tag{29}$$

It is worth noting that, given the definition of the control normal vector in Equation 26, Equation 28 does not exhibit an explicit dependency on $\mathbf{v}$. Specifically, the control vector is independent of the velocity. In this scenario, the control law is saturated solely due to the constraint on the control cone angle α. As previously detailed, the clock angle has no restrictions and therefore always adheres to the optimal control law.

A dependency on $\mathbf{v}$ arises only if both control angles are saturated, preventing either from reaching its optimal value. In this case, the control law given by Equation 22 is no longer valid, and consequently, neither is Equation 26, which leads to Equation 28. However, this scenario is not physically realistic, as the clock angle is not subject to any constraints.

Moreover, when the cone angle α is also unconstrained and adheres to the optimal control law, i.e., $\alpha^* = \alpha^\star$, it can be verified that

$$-\frac{\beta\mu}{r^4}\left[\frac{\partial\mathbf{n}}{\partial\mathbf{r}}\right]^T_{(\alpha,\delta)=(\alpha^*,\delta^*)} (\mathbf{r}\cdot\mathbf{n}(\alpha^*,\delta^*))\,(2(\mathbf{n}(\alpha^*,\delta^*)\cdot\boldsymbol{\lambda}_v)\mathbf{r} + (\mathbf{r}\cdot\mathbf{n}(\alpha^*,\delta^*))\boldsymbol{\lambda}_v) = \mathbf{0} \tag{30}$$

Notice the distinction in the nomenclature $\alpha^\star$ instead of α^*, as this control input may be subject to saturation, although it is not constrained in this particular instance. Only under this specific condition of no constraint does $\alpha^\star$ equate to α^*.

Therefore, in the absence of any constraints imposed on the control inputs, and if they consequently follow the optimal control law $(\alpha,\delta) = (\alpha^*,\delta^*)$, the Euler–Lagrange equations defining the evolution of the costate vectors are

$$\begin{aligned} \dot{\mathbf{x}} &= \mathbf{f}(\mathbf{x},\mathbf{u},t) \\ \dot{\boldsymbol{\lambda}}_r &= -\left(3\frac{\mu}{r^5}\mathbf{r}\,\mathbf{r}^T - \frac{\mu}{r^3}\mathbf{I}_{3x3}\right)\boldsymbol{\lambda}_v - 2\frac{\beta\mu}{r^4}(\mathbf{r}\cdot\mathbf{n})\,(\mathbf{n}\cdot\boldsymbol{\lambda}_v)\left[\mathbf{n} - \frac{2(\mathbf{r}\cdot\mathbf{n})\mathbf{r}}{r^2}\right] \\ \dot{\boldsymbol{\lambda}}_v &= -\boldsymbol{\lambda}_r \end{aligned} \tag{31}$$

Regarding the validation of the results and exploiting time-optimal properties, it is a known result from the Euler–Lagrange necessary conditions for optimal control that in a time-optimal solution for this two-body problem with solar sail propulsion and saturated control, neither $\mathbf{f}(\mathbf{x}, \mathbf{u}, t)$ nor $l(\mathbf{x}, \mathbf{u}, t)$ explicitly depend on time [39]. Consequently, $H(t)$ is a constant, denoted as

$$H(t) = H \tag{32}$$

Therefore, the conservation of the Hamiltonian in both scenarios (saturation and nonsaturation) is a well-known result derived from the Euler–Lagrange necessary conditions for optimal control, which offers valuable validation for the obtained results. Ensuring it helps not only validate the results but note that confirms that all the Euler–Lagrange conditions are correctly derived as well as the optimal control law.

C. Interior point constraint: visiting several asteroids

Once the problem of rendezvous with an asteroid, whose motion is determined by its ephemeris, has been thoroughly addressed, one might consider scenarios involving flyby maneuvers. This spacecraft operation implies passing proximally to a body, in this case, another asteroid of interest, allowing for its exploration and observation. Given the reachability of an asteroid ensemble, a new mission can be undertaken: the flyby of an asteroid after encountering several asteroids for flyby operations. In the context of optimal control theory, performing an intermediate flyby involves imposing a constraint at an interior point.

For example, a mission aimed at finding a time-optimal trajectory intends to perform a flyby maneuver with a primary asteroid ($\mathbf{r}_a$, $\mathbf{v}_a$) while executing a flyby operation with a secondary asteroid ($\mathbf{r}_{fb}$) along the trajectory towards the final destination. Consequently, the problem faced is no longer a contour one but rather a multi-point problem is established.

An interior point constraint at time t_1 is defined as follows:

$$\mathbf{N}[t_1, \mathbf{x}(t_1)] = 0 \quad t_0 < t_1 < t_f \tag{33}$$

Here, $\mathbf{N}(t_1) \in \mathbb{R}^m$, and m represents the number of constraints.

Since the spacecraft must perform a flyby at a specific asteroid, the interior constraint $\mathbf{N}(t_1)$ ($m = 3$, position condition) is

$$\mathbf{N}(t_1) : \mathbf{r}_{fb}(t_1) - \mathbf{r}(t_1) = 0 \tag{34}$$

$\mathbf{\Psi}_{fb}(t_1) = [\mathbf{r}_{fb}(t_1)\ \mathbf{v}_{fb}(t_1)]^T$ describes the motion (position and velocity) of the asteroid at which the flyby is intended to occur.

There are significant consequences of this interior point constraint. Functions that were expected to remain continuous are no longer continuous, and the Pontryagin Minimization Principle defines the jump in Equation 35 [35] which establishes some conditions in time t_1 which must fulfil a process $(\mathbf{x}^*, \mathbf{u}^*)$ to be optimal:

$$\begin{aligned} \lambda_i(t_1^-) &= \lambda_i(t_1^+) + \boldsymbol{\pi}^T \frac{\partial \mathbf{N}}{\partial x_i(t_1)}(t_1^+, \mathbf{x}(t_1)) \quad i = 1, .., m \\ H(t_1^-) &= H(t_1^+) - \boldsymbol{\pi}^T \frac{\partial \mathbf{N}}{\partial t_1} \end{aligned} \tag{35}$$

where t_1^- and t_1^+ represent the times immediately before and after the interior point constraint.

Here, m new constraints are incorporated, accompanied by m new unknown multipliers ($\boldsymbol{\pi}$), whose values are determined such that the constraints are satisfied at point t_1. Note that there is one additional unknown, time t_1, which is free. Therefore, an additional equation is necessary to close the zero-finding problem: the discontinuity or jump in the Hamiltonian at time t_1.

In general, even if the adjoint vector and the Hamiltonian are discontinuous, the state itself does not undergo jumps due to the inherent nature of its dynamics. Consequently, continuity in position at the flyby point is assured:

$$\mathbf{r}(t_1^-) = \mathbf{r}(t_1^+) \tag{36}$$

As a result, the zero-finding problem initially formulated for a simple time-optimal rendezvous mission in Equation 15 now encompasses a single flyby. This entails determining the unknowns $(\boldsymbol{\lambda}_0, \boldsymbol{\pi}, t_1, t_f)$ such that, when incorporated into the state and costate dynamics (12) and consistent with the costate discontinuity defined in Equation 35, the following conditions are fulfilled: the intermediate flyby position constraint at t_1, the terminal constraints (six final equations for rendezvous at t_f), the Hamiltonian discontinuity defined in Equation 35, and finally, the transversality condition. This system of 11 equations is expressed as shown in Equation 37.

$$\begin{aligned} \mathbf{r}_{fb}(t_1) - \mathbf{r}(t_1) &= 0 \\ \mathbf{r}_a(t_f) - \mathbf{r}(t_f) &= 0 \\ \mathbf{v}_a(t_f) - \mathbf{v}(t_f) &= 0 \\ H(t_1^-) - H(t_1^+) + \boldsymbol{\pi}^T \left(\mathbf{v}_{fb}(t_1) - \mathbf{v}(t_1)\right) &= 0 \\ H(t_f) - \boldsymbol{\lambda}(t_f)^T \dot{\boldsymbol{\Psi}}(t_f) &= 0 \end{aligned} \tag{37}$$

In order to partially reduce the problem's complexity and consequently weaken the dependency on the costate vectors (initial and those corresponding to the constraints at interior points), a mission involving only flybys is considered. Thus, in this case, the final rendezvous does not occur, and instead, a final flyby is the chosen maneuver.

Consequently, the optimal control problem must be adjusted in accordance with this new final condition. While the dynamic differential equations governing the TPBVP (Equation 31) remain unchanged, only the final conditions are modified. With the removal of the rendezvous condition, the spacecraft does not need to match the asteroid's velocity at the final encounter. Therefore, the terminal constraint (15b), which imposes a free final velocity, is replaced by new Euler–Lagrange necessary conditions for optimal control, demanding

$$\boldsymbol{\lambda}_v(t_f) = \mathbf{0} \tag{38}$$

This new final condition is then integrated into the DAEs.

IV. Implementation

Addressing the practical implementation of this theoretical resolution entails numerous challenges. The significant dependence on the initial guess provided to the solver, which is typical when employing an indirect approach, constitutes the main challenge encountered and can result in poor solver convergence. Section IV.A offers a comprehensive explanation of the integration of various techniques aimed at ensuring an effective resolution method. Furthermore, Section IV.B delves into the selection of the lightness number parameter and the continuation scheme, both essential for conducting minimum-time mission analysis from Earth.

A. Indirect approach convergence

The first important issue that arises in the solution of nonlinear problems is scaling. It is known that a poorly scaled problem can lead to either extremely slow convergence or divergence [38]. Since in this problem the relative size of variables is vastly different, units should be transformed into a relatively similar scale. For this purpose, dimensionless distance, time and velocity units are introduced. These units are selected according to the Sun-Earth two-body problem.

Additionally, this problem exhibits a pronounced dependence of convergence on the initial costate vector. The solution of the shooting functions is notably sensitive to variations in the initial values, as highlighted by [33]. Both [33] and [22] employ a normalization method for the initial costates, which is elaborated upon in the literature [36]. In this case, a costate initialization method is employed to obtain better estimates. This method is based on the idea that in the neighborhood of the initial time instant, the evolution of the costate vector $\boldsymbol{\lambda}(t)$ can be approximated by a first-order Taylor series expansion as presented in [40] and [41] to obtain better estimates.

In order to solve the TPBVP resulting in a dimensionless system of nonlinear equations, the *fsolve* root-finding algorithm in MATLAB is employed. During each iteration of the zero-finding problem, the solver utilizes the initial Lagrange multiplier vector $\boldsymbol{\lambda}_0$ (position and velocity) and the final mission time (t_f) to seek a root of the system of DAEs, which includes Equation 15. Facilitating this process necessitates the determination of the final position and velocity of

the target asteroid, for which the ephemeris is calculated using the sliding Lagrange Polynomials function (Equation 6).

The resolution of the nonlinear differential system can be improved in terms of accuracy and computational speed when adding the analytical Jacobian matrix of the system. For this purpose, it is necessary to compute and integrate with Equation 31 the state transition matrix (STM) $\Phi(\mathbf{x}_0, t_0; t)$, which is the Jacobian matrix of the flow correspondent to the dynamics of the problem (scalar 144 ODEs). The variational approach provides the integration of the STM

$$\dot{\Phi}(t_0, t) = A(t)\,\Phi(t_0, t) \qquad \Phi(t_0, t_0) = \mathbf{I} \tag{39}$$

where $A(t) = \left[\dfrac{\partial \mathbf{f}}{\partial \mathbf{x}}\right]_{\mathbf{x}=\mathbf{x}^*}$.

$$A(t) = \begin{bmatrix} \mathbf{0}_{3x3} & \mathbf{I}_{3x3} & \mathbf{0}_{3x3} & \mathbf{0}_{3x3} \\ \left(3\dfrac{\mu}{r^5}\mathbf{r}\,\mathbf{r}^T - \dfrac{\mu}{r^3}\mathbf{I}_{3x3}\right) + \dfrac{\partial \mathbf{a}_n}{\partial \mathbf{r}} & \mathbf{0}_{3x3} & \mathbf{0}_{3x3} & \dfrac{\partial \dot{\mathbf{r}}}{\partial \boldsymbol{\lambda}_v} \\ \dfrac{3\mu}{r^5}\left(\dfrac{5\mathbf{r}^T\boldsymbol{\lambda}_v}{r^2}\mathbf{r}\mathbf{r}^T - (\boldsymbol{\lambda}_v\mathbf{r}^T + \mathbf{r}^T\boldsymbol{\lambda}_v\mathbf{I}_{3x3} + \mathbf{r}\boldsymbol{\lambda}_v^T)\right) + \dfrac{\partial \dot{\boldsymbol{\lambda}}_r}{\partial \mathbf{r}} & \mathbf{0}_{3x3} & \mathbf{0}_{3x3} & \left(3\dfrac{\mu}{r^5}\mathbf{r}\,\mathbf{r}^T - \dfrac{\mu}{r^3}\mathbf{I}_{3x3}\right) + \dfrac{\partial \dot{\boldsymbol{\lambda}}_r}{\partial \boldsymbol{\lambda}_v} \\ \mathbf{0}_{3x3} & \mathbf{0}_{3x3} & -\mathbf{I}_{3x3} & \mathbf{0}_{3x3} \end{bmatrix} \tag{40}$$

whose terms which are not explicitly indicated can be found in the Appendix VI.A. In this analytical development, it is fundamental to use the chain rule.

Consequently, the Jacobian matrix of the system $\mathcal{J} = [\mathcal{J}_{\lambda_{r_0}}\ \mathcal{J}_{\lambda_{v_0}}\ \mathcal{J}_{t_f}]$ corresponding to a single rendezvous asteroid problem is given by Equation 59 in the Appendix.

When incorporating intermediate flyby constraints, the reliance on the initial guess for the unknowns becomes even more pronounced. This dependence extends not only to the initial costate vector but also to the intermediate position costate, which defines the discontinuity in the Euler–Lagrange dynamics, denoted as $\boldsymbol{\pi}$.

Notice that for each intermediate encounter, four extra unknowns are included in the problem. To mitigate the dependency on the initial unknown guess and enhance algorithm convergence, it is essential to utilize the analytical Jacobian matrix of the problem. However, due to the size of such an analytical expression, it is not included in this paper. Computing this matrix involves obtaining the STM for a problem with interior constraints. Nevertheless, the discontinuities associated with p intermediate constraints (assuming p flybys) prevent direct computation of the matrix as before.

In the event of an intermediate flyby at t_j, as described in [38], $\Phi(t_j, t)$ maps states along a continuous orbit. However, if a flyby is to be performed at time t_j, the STM across such a discontinuity must be determined. Fortunately, in this scenario, its computation is straightforward. Despite a discontinuity in the position costates, the remainder of the dynamics remains continuous, and there is no switching function since the intermediate constraint does not depend on

the state or costate vector. Therefore, the STM between the times immediately before and after the flyby is the identity matrix.

$$\Phi(t_j^-, t_j^+) = \mathbf{I}_{12x12} \tag{41}$$

Equation 41 holds under the assumption that asteroid gravity and other perturbations are neglected. When considering the influence of the asteroid on the spacecraft's motion, the dynamics of the problem (Equation 7) are modified. However, this effect has been neglected due to the nature of NEA considered. Among the asteroids analyzed in the results (Table 1), one of the largest is 2009 CV, with a diameter of 47 meters. Given that its distance from the Sun is on the order of 1 AU, the sphere of influence of this asteroid is approximately of the order of 10^{-6} % relative to the minimum distance between the spacecraft and the Sun along its optimal trajectory, at the optimal departure date indicated in Table 1. This effect could be easily corrected using a feedback control mechanism, although this is beyond the scope of the present paper.

Therefore, having p intermediate flybys performed at times t_j with $j = 1, ..., p$ the composition of the STM gives

$$\Phi(t_0, t) = \Phi(t_p, t)\Phi(t_{p-1}, t_p)...\Phi(t_1, t_2)\Phi(t_0, t_1) \tag{42}$$

where $\Phi(t_j, t_{j+1})$ is integrated with initial conditions $\Phi(t_j, t_j) = \mathbf{I}_{12x12}$ and $\mathbf{x}(t_j)$ computed as the final conditions at t_j^- with the discontinuity applied at the position costate

$$\boldsymbol{\lambda}_r(t_j^-) = \boldsymbol{\lambda}_r(t_j^+) + \boldsymbol{\pi}_j \tag{43}$$

Specifically, when incorporating an intermediate flyby to another asteroid into the mission, the optimal control problem is adjusted by introducing four new unknowns: the flyby time t_1 and the costate position vector associated with this interior point constraint, denoted as $\boldsymbol{\pi}$. The computation of the Jacobian matrix detailed in column matrices 60a, 60b, 60c, 60d and 60e (Appendix) corresponding to the Equation System 37 becomes straightforward.

Identical results are obtained numerically (with finite differentiation in order to compute the Jacobian) or providing the Jacobian of the system (variational approach for STM). Nevertheless, the speed of the solver iteration computation once provided the Jacobian is noticeably quicker.

B. Lightness number and continuation scheme

The lightness number β exerts substantial influence over the resulting time-optimal trajectory. It is essential to recognize that this parameter describes the acceleration capability of the sail fundamentally shaping the feasible orbital maneuvers for a given spacecraft. Consequently, β serves as a design parameter highly dependent on the areal density of

the sail. The primary goal is to maintain alignment with the article in the literature [1], which computes the reachability with an envelope of asteroids but using electric low-thrust propulsion. Simultaneously, an additional objective is to approach a realistic model and a design similar to that of the NEA scout mission, wherein a 6U CubeSat is employed.

In this way, the value of β, which partially achieves the same propulsion capability as the figures found in the literature, is $\beta = 0.04$. This value is significant since, according to [23], a solar-sail lightness number in the range $\beta = 0.025 - 0.04$ corresponds to a 12U spacecraft. The lightness number of the sail employed for the NEA Scout mission is similar to the result obtained (~ 0.02).

Creating the (t_0, TOF) curves involves discretizing the selected launch window spanning 2025 and 2027 (two-year departure window). The time window is divided into a grid with an initial half-day time step. To efficiently tackle the numerous time-optimal problems, an agile strategy has been devised, inspired by the methodology implemented in Topputo et al.'s work [1]).

The continuation strategy, illustrated in Figure 4, is designed to systematically explore and solve the two-year window. By reducing the computational load and seeking rapid convergence, this approach offers a structured means to scan the solution space. To initiate the process, the departure time window is discretized with a half-day time step (h).

$$t_i = t_0 + h \cdot i \tag{44}$$

with $i = 1, ..., N_h$, being N_h the number of points of the mission grid.

Once the time-optimal solution for a given $t_i = t_0$ is obtained, the subsequent solution for t_{i+1} is sought, where the initial time increment is set to half a day. This search for the next step utilizes the previous solution, including the costate vector and final time. If convergence is achieved, the continuation scheme progresses. In the event of non-convergence, the time step h is halved to $h' = h/2$, and a new point on the time-optimal curve is targeted, specifically $t_i' = t_i + h'$.

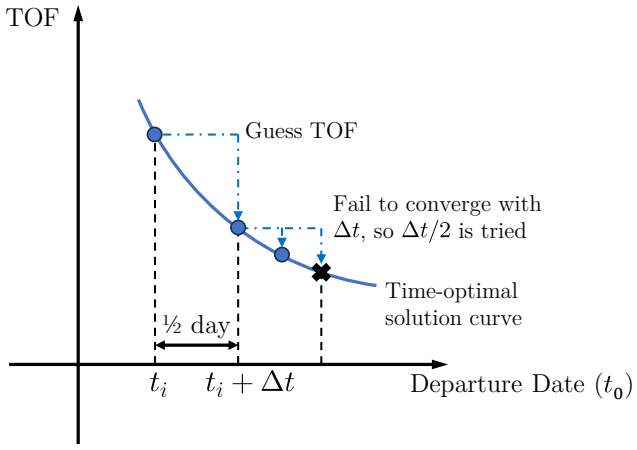

Fig. 4 Continuation strategy.

This process continues with successive halving of the time step until convergence is reached. Once obtained, the departure time for which the solution did not initially converge (t_{i+1}) is revisited. If it now converges, the continuation proceeds with the original time step. Otherwise, the process recommences from the new point t_i', leading to a new halved time step of $h' = (t_{i+1} - t_i')/2$. Consequently, the step size progressively diminishes while approaching the new point on the time grid.

Using this procedure the final departure date is reached obtaining a nonuniform discretization time grid specially at the time zones where solutions show fairly little convergence.

V. Results

To demonstrate the computational capabilities of this solar sail trajectory optimization tool, several results are addressed. Firstly, in Section V.A, the algorithm is validated exploring time-optimal missions to the dwarf planet Ceres using a maximum cone angle constraint. This section provides a detailed interpretation of the obtained solutions. Subsequently, the analysis of minimum-time missions from Earth over several years is computed and presented in tables in Section V.B. Finally, Section V.C presents the results obtained from finding time-optimal missions that involve visiting or encountering more than one asteroid, incorporating intermediate flyby maneuvers.

A. Validation: Mission to Ceres

The analysis focuses on a solar sail transfer initiated from Earth, for which ephemeris data provided by the SPICE toolbox is utilized. The journey commences on January 1, 2027, TDB (Barycentric Dynamical Time). Solar sail propulsion is employed to gradually increase the spacecraft's energy until it reaches Ceres in a rendezvous transfer. For this particular simulation, the lightness number is fixed at $\beta = 0.1$. Figure 5 (left) illustrates the optimal-time solution in terms of the minimum-time transfer trajectory obtained for rendezvous with the dwarf planet Ceres, with $\alpha_{max} = 40\,\text{deg}$. Figure 7 (left) depicts the evolution and saturation of the cone angle. The minimum time achieved is '2032 NOV 21 02:32:52.8320' (2151 days). Figure5 (right) illustrates the evolution of the solar sail normal vector, whereas Figure 6 presents the ecliptic plane view and the YZ-plane view of the control vector along the trajectory. Various validations, including the constancy of the Hamiltonian shown in Figure 7 (right), demonstrate the effectiveness of the algorithm.

B. Analysis of Minimum-Time Missions from Earth

Once this example has been carried out, showing the computational capabilities of this MATLAB tool created from an indirect variational approach, a study of the reachable targets from Earth is established. As the solar sail propulsion model is designed and scaled so that the time-optimal mission duration is similar, the asteroid list presented in [1] can be used as mission target and a similar table as the one presented in its appendix can be constructed.

Time-optimal transfers are ranked in Table 1. In the table the following columns are detailed: # the position

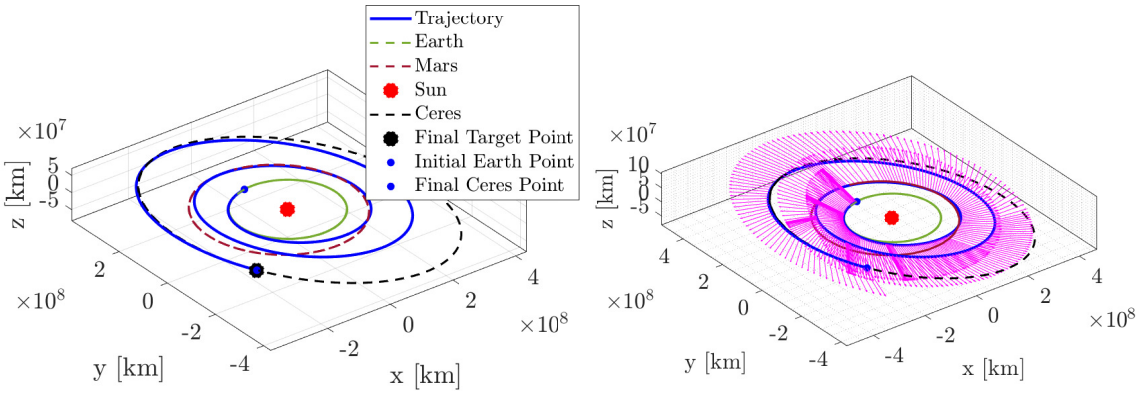

Fig. 5 Minimum-time solution for the rendezvous with Ceres dwarf planet, $\beta = 0.1$: 3D ecliptic view (left) and normal vector to the sail (right), J2000 frame centered in SSB.

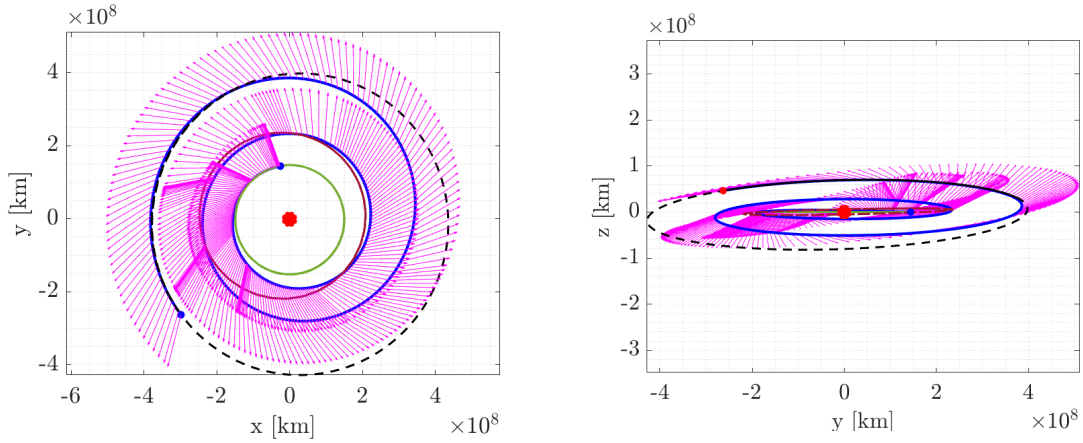

Fig. 6 Minimum-time solution for the rendezvous with Ceres dwarf planet, $\beta = 0.1$, normal vector to the sail: XY ecliptic view (left) and YZ ecliptic view (right), J2000 frame centered in SSB.

in the ranking; *Name* asteroid name; TOF_{min} minimum transfer time expressed in days; and the *Departure Date* (DD/MM/YYYY) correspondent to the time-optimal point in the curve.

In Figure 8, the minimal time of flight (TOF) is plotted against the corresponding optimal departure date, illustrating the global optimal solution for the entire envelope of considered asteroids for the departure windows under consideration: 2025-2027.

C. Visiting several asteroids

Finally, a comprehensive exploration lies in the investigation of time-optimal missions involving multiple asteroids, employing the theoretical framework developed in Section III.C. However, owing to the substantial computational demands of such multi-target missions, the results are only presented for scenarios involving three target asteroids along the trajectory. The selected asteroids are: 2010 UE51, 2009 CV, and 2014 JR24. The analysis scrutinizes the 3! = 6

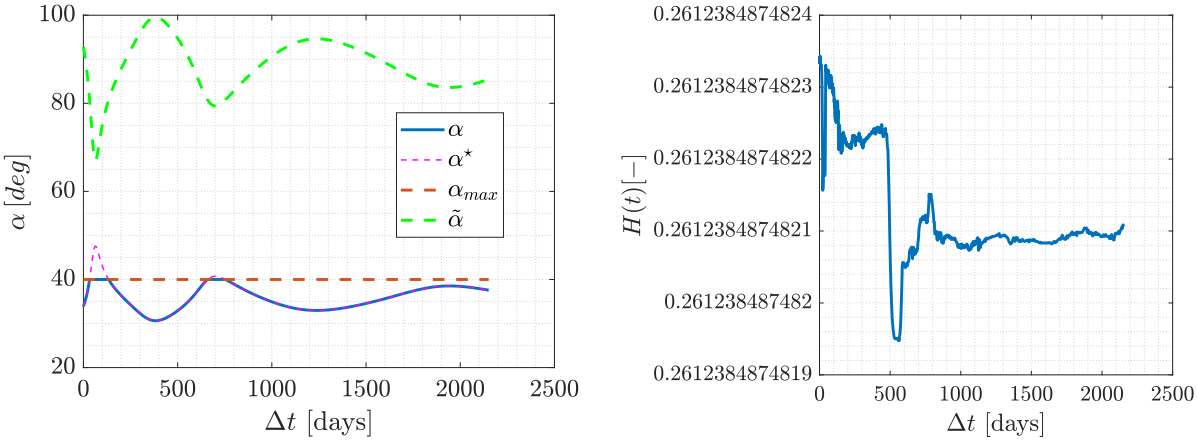

Fig. 7 Minimum-time solution, $\beta = 0.1$ and $\alpha_{max} = 40$ deg: cone angle evolution (left) and Hamiltonian (right).

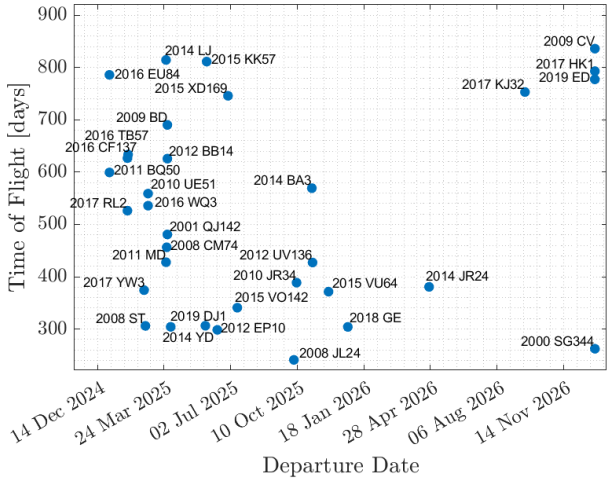

Fig. 8 Analysis of minimum-time missions from Earth: 2025-2027 departure window.

possible trajectories to visit all three asteroids along with their respective time-optimal missions.

Regarding the determination of an initial guess, a “semi-random" guess generator is employed. Notably, the unknowns pertinent to this problem requiring initial estimations are

$$\mathbf{z}_0 = [\boldsymbol{\lambda}_0, \boldsymbol{\pi}_1, \boldsymbol{\pi}_2, t_{fb1}, t_{fb2}, t_f]$$

where $\boldsymbol{\pi}_1$ and t_{fb1} are the position costate and time corresponding to the first flyby, and $\boldsymbol{\pi}_2$ and t_{fb2} correspond to the second flyby operation.

For each possible trajectory, to determine a suitable guess, the two-asteroid problem must be solved for the first two bodies that the spacecraft encounters. This solution provides an idea about the initial order of the costate vector. For instance, when solving the first possible trajectory (Table 2) between the three selected asteroids, it is necessary first

Table 1 Time-optimal Earth-asteroid transfer solution between 2025 and 2027, $\beta = 0.04$.

#	Name	TOF	Dep. Date	#	Name	TOF	Dep. Date
1	2008 JL24	240.99	05/10/2025	**18**	2016 WQ3	535.79	28/02/2025
2	2000 SG344	262.29	31/12/2026	**19**	2010 UE51	558.93	28/02/2025
3	2012 EP10	298.41	12/06/2025	**20**	2014 BA3	569.30	01/11/2025
4	2018 GE	304.03	25/12/2025	**21**	2011 BQ50	599.32	01/01/2025
5	2014 YD	304.18	03/04/2025	**22**	2012 BB14	625.73	29/03/2025
6	2008 ST	306.02	24/02/2025	**23**	2016 CF137	626.70	28/01/2025
7	2019 DJ1	306.32	25/05/2025	**24**	2016 TB57	633.65	29/01/2025
8	2015 VO142	340.81	12/07/2025	**25**	2009 BD	690.17	29/03/2025
9	2015 VU64	371.42	26/11/2025	**26**	2015 XD169	745.85	28/06/2025
10	2017 YW3	374.36	22/02/2025	**27**	2017 KJ32	753.1	17/09/2026
11	2014 JR24	380.56	26/04/2026	**28**	2019 ED	777.28	31/12/2026
12	2010 JR34	388.63	09/10/2025	**29**	2016 EU84	785.88	01/01/2025
13	2012 UV136	427.15	02/11/2025	**30**	2017 HK1	792.99	31/12/2026
14	2011 MD	427.71	27/03/2025	**31**	2015 KK57	811.23	27/05/2025
15	2008 CM74	456.27	28/03/2025	**32**	2014 LJ	814.41	27/03/2025
16	2001 QJ142	480.76	29/03/2025	**33**	2009 CV	835.98	31/12/2026
17	2017 RL2	526.26	28/01/2025				

to find the optimal trajectory to visit and flyby 2010 UE51 and 2009 CV. The final minimum-time is '2028 JUN 06 05:39:33.8750' (1252 days) with the intermediate flyby performed at '2026 APR 24 13:39:28.6882' (478 days). This optimal trajectory is depicted in Figure 9. The unknown encounter times are generated randomly, exploring various combinations of random flyby times until the DAEs system is solved.

As previously discussed, computing the time-optimal solution for a simple rendezvous problem exhibits rapid convergence with minimal dependence on the initial guess provided to the solver, thanks to the techniques outlined in Section IV.A. However, this immediate approach cannot be directly applied to a multiple-target problem, as the number of unknown variables increases significantly. Even when providing the analytical Jacobian matrix for the three-body target transfer, the dependence on the initial guess can, in some cases, lead to excessively long computational times (ranging from seconds to several hours) to find a locally optimal solution.

To mitigate this issue, after the initial guess is generated, the unknown encounter times are assigned randomly, and a systematic sweep is performed to explore various encounter time combinations until a valid solution is obtained. By employing this semi-random initial guess estimator, a MATLAB loop iterates until a solution is found. This approach effectively reduces the computational time required to determine a time-optimal solution to a level comparable to the results presented in Part V.A or V.B.

Finally, all possible combinations to construct the trajectory encountering these three NEAs are computed, and the results are presented in Table 2. The optimal sequence to visit the three asteroids is the one depicted in Figure 10,

whose optimal trajectory is described in Table 2 in terms of flyby times.

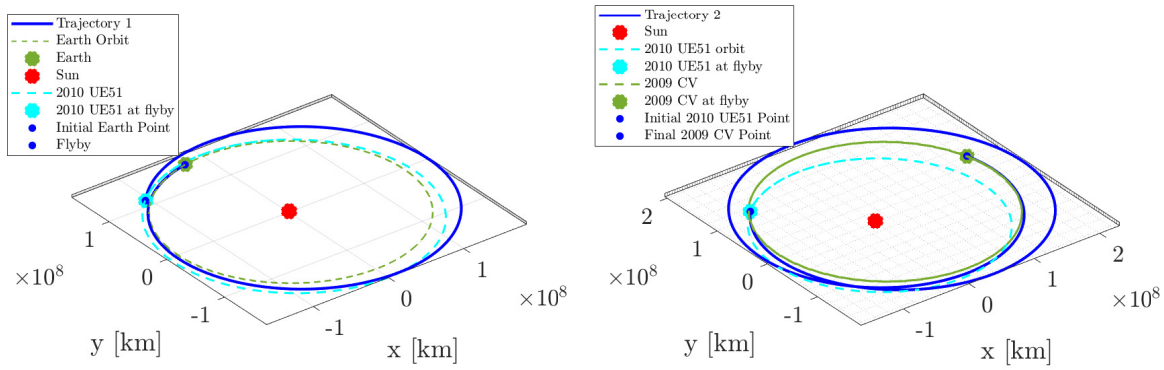

(a) Flyby to 2010 UE51. **(b) Flyby to 2009 CV.**

Fig. 9 Time-optimal trajectory: Earth-2010 UE51-2009 CV transfer solution, $\beta = 0.04$, wrt Ecliptic J2000, centered on SSB.

VI. Conclusions

The primary contribution of this article was based on [1] wherein an evaluation of the attainable set of target NEAs was conducted. In this work, time-optimal solar sail-based propulsion optimisation problems were solved. Consequently, the computation of optimal or minimal trajectories within this envelope requires the application of continuous-time optimal theory.

Addressing this problem entails numerous challenges, the practical implementation of this theoretical resolution involves the incorporation of various techniques to ensure an effective resolution method. These techniques include the complete analytical formulation of the problem's Jacobian matrix, an initial guess generator and a continuation strategy. The continuation strategy is designed to systematically explore the departure window when calculating the reachability from Earth. Assessing the reachability requires addressing thousands of individual asteroid rendezvous problems, owing to the departure time grid and the multitude of selected asteroids.

In this model, a geometrically and dynamically ideal solar sail has been considered. These assumptions simplify the resolution of the optimal control law and the overall sail design. Although their relaxation would be necessary for a more complex, real-world application, the optimization framework remains valid, offering a providing the tools for preliminary time-optimal mission analysis involving multiple targets.

The most significant achievement lies in demonstrating the algorithm's effectiveness in uncovering optimal trajectories and control laws for missions exploring various NEAs using a propulsive solar sail model. The developed algorithm proves to be a versatile tool capable of generating quantitative outcomes for missions involving trajectories with multiple flyby encounters. Importantly, such intermediate flybys have not been addressed in solar sail optimal control

Table 2 Time-optimal Earth, 2009 CV, 2010 UE51, and 2014 JR24 transfer solutions, $\beta = 0.04$.

Combination	Body	Event	Time (TDB)	TOF [days]
1	Earth	Departure	'2025 JAN 01 00:00:00.0000'	-
	2010 UE51	Flyby 1	'2026 JUN 07 20:02:15.3584'	522.83
	2009 CV	Flyby 2	'2028 JUN 05 21:12:38.3238'	1.2519e+03
	2014 JR24	Flyby 3	'2030 JAN 17 23:07:09.6380'	1.8430e+03
2	Earth	Departure	'2025 JAN 01 00:00:00.0000'	-
	2009 CV	Flyby 1	'2027 MAY 13 04:02:09.0256'	862.16
	2010 UE51	Flyby 2	'2028 DEC 01 02:11:47.9442'	1.4301e+03
	2014 JR24	Flyby 3	'2032 APR 09 17:56:35.2141'	2.6557e+03
3	Earth	Departure	'2025 JAN 01 00:00:00.0000'	-
	2010 UE51	Flyby 1	'2027 AUG 04 18:16:05.1547'	945.76
	2014 JR24	Flyby 2	'2029 MAR 21 03:32:07.6223'	1.5401e+03
	2009 CV	Flyby 3	'2030 JUL 01 21:52:31.0733'	2.0079e+03
4	Earth	Departure	'2025 JAN 01 00:00:00.0000'	-
	2009 CV	Flyby 1	'2027 OCT 20 12:11:43.6085'	1.0225e+03
	2014 JR24	Flyby 2	'2028 SEP 12 20:57:00.5645'	1.3509e+03
	2010 UE51	Flyby 3	'2029 NOV 09 13:12:29.7546'	1.7736e+03
5	Earth	Departure	'2025 JAN 01 00:00:00.0000'	-
	2014 JR24	Flyby 1	'2026 FEB 07 16:53:02.4394'	402.70
	2009 CV	Flyby 2	'2027 DEC 05 03:44:53.6496'	1.0682e+03
	2010 UE51	Flyby 3	'2029 MAR 22 20:47:49.5225'	1.5419e+03
6	Earth	Departure	'2025 JAN 01 00:00:00.0000'	-
	2014 JR24	Flyby 1	'2027 MAR 10 13:23:55.9357'	798.56
	2010 UE51	Flyby 2	'2030 APR 05 18:00:03.3832'	1.9208e+03
	2009 CV	Flyby 3	'2033 FEB 08 21:05:46.7084'	2.9609e+03

problems documented in existing literature. Thanks to the various techniques expounded, the algorithm efficiently determines optimal times for proposed target missions while mitigating the initial high dependence on existing initial guess parameters.

Acknowledgements

R. Vazquez and G. Zamora gratefully acknowledge support by grant TED2021-132099B-C33, funded by MICIU/AEI/10.13039/501100011033 and by "FEDER A way of making Europe."

Appendix

A. Computation of $A(t)$ matrix

In this appendix, it is explicitly detailed the analytic computation of the different terms appearing in matrix $A(t)$ (Equation 40). This matrix allows to integrate the state transition matrix whose differential equation is an ODE with time

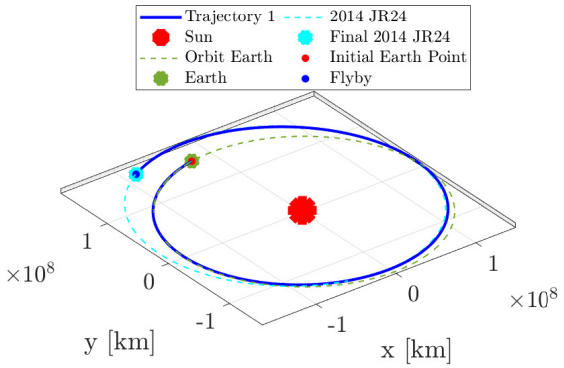

(a) Flyby to 2014 JR24.

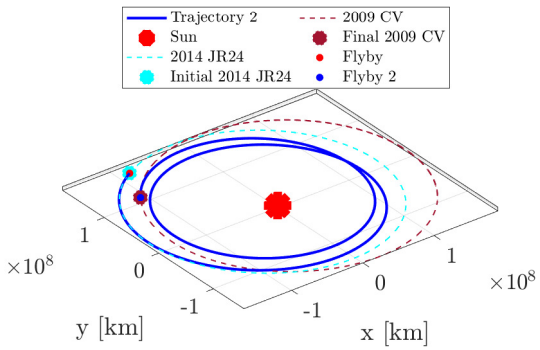

(b) Flyby to 2009 CV.

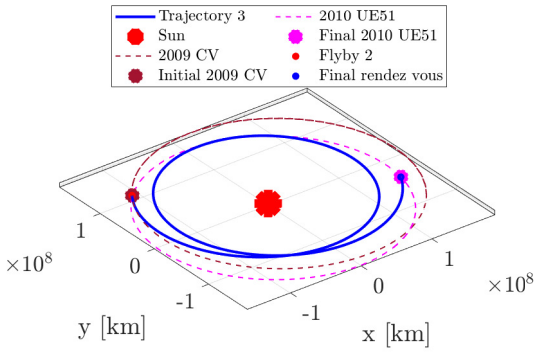

(c) Rendezvous to 2010 UE51.

Fig. 10 Time-optimal Earth-2014 JR24-2009 CV-2010 UE51 transfer solution, $\beta = 0.04$, wrt Ecliptic J2000, centered on SSB.

varying coefficients (39). In this analytical development, as it is found in the following expressions, it is fundamental to make use of the chain rule, when deriving the different terms, in order to understand and make simple to work with the complex expressions obtained.

In matrix $A(t)$ (40)

$$\frac{\partial \mathbf{a}_n}{\partial \mathbf{r}} = \mu\beta \left[\frac{2\mathbf{n}^T\mathbf{r}}{r^4}\mathbf{n}\mathbf{n}^T - 4\frac{(\mathbf{n}^T\mathbf{r})^2\mathbf{n}}{r^6}\mathbf{r}^T + \left(2\frac{\mathbf{r}^T\mathbf{n}}{r^4}\mathbf{n}\mathbf{r}^T + \frac{(\mathbf{r}^T\mathbf{n})^2}{r^4}\mathbf{I}_{3x3}\right)\frac{\partial \mathbf{n}}{\partial \mathbf{r}} \right] \tag{45}$$

where

$$\frac{\partial \mathbf{n}}{\partial \mathbf{r}} = \frac{\sin(\alpha+\tilde{\alpha})}{\sin\tilde{\alpha}}\left(\frac{\mathbf{I}_{3x3}}{r} - \frac{\mathbf{r}\mathbf{r}^T}{r^3}\right) + \hat{\mathbf{i}}_r\left(\frac{\frac{\partial(\sin(\alpha+\tilde{\alpha}))}{\partial \mathbf{r}}\sin\tilde{\alpha} - \frac{\partial(\sin\tilde{\alpha})}{\partial \mathbf{r}}\sin(\alpha+\tilde{\alpha})}{\sin(\tilde{\alpha})^2}\right) \tag{46}$$

$$+ \hat{\boldsymbol{\lambda}}_v\left(\frac{\frac{\partial(\sin\alpha)}{\partial \mathbf{r}}\sin\tilde{\alpha} - \frac{\partial(\sin\tilde{\alpha})}{\partial \mathbf{r}}\sin\alpha}{\sin(\tilde{\alpha})^2}\right)$$

where

$$\frac{\partial(\sin(\alpha+\tilde{\alpha}))}{\partial \mathbf{r}} = \frac{\partial(\sin\alpha)}{\partial \mathbf{r}}\cos\tilde{\alpha} + \sin\alpha\left(-\frac{\sin\tilde{\alpha}}{\cos\tilde{\alpha}}\right)\frac{\partial(\sin\tilde{\alpha})}{\partial \mathbf{r}} + \sin\tilde{\alpha}\left(-\frac{\sin\alpha}{\cos\alpha}\right)\frac{\partial(\sin\alpha)}{\partial \mathbf{r}} + \cos\alpha\frac{\partial(\sin\tilde{\alpha})}{\partial \mathbf{r}} \tag{47}$$

$$\frac{\partial(\sin\tilde{\alpha})}{\partial \mathbf{r}} = \frac{\cos\tilde{\alpha}}{\sin\tilde{\alpha}}\left(\frac{\mathbf{r}^T\boldsymbol{\lambda}_v}{r^3\lambda_v}\mathbf{r} - \frac{\boldsymbol{\lambda}_v}{\lambda_v r}\right) \tag{48}$$

$$\frac{\partial(\sin\alpha)}{\partial \mathbf{r}} = -\left(\frac{12\,t_0\,t_{11}\,t_{15}}{16\,t_{16}\,t_8}\mathbf{r} - \frac{3\,t_{17}}{4\,t_8\,t_3}\boldsymbol{\lambda}_v + \frac{9\,t_0\,t_{11}\,t_{15}}{4\,t_{16}\,t_{18}}\mathbf{r} - \frac{9\,t_{17}}{4\,t_{18}\,t_3}\boldsymbol{\lambda}_v\right) \tag{49}$$

where

$$t_0 = \mathbf{r}^T\boldsymbol{\lambda}_v \qquad t_3 = r\lambda_v \qquad t_8 = \tan(\tilde{\alpha})^2 \qquad t_9 = \left(8 + \tfrac{9}{t_8}\right)^{1/2}$$

$$t_{10} = \tfrac{3}{\tan\tilde{\alpha}} + \tfrac{t_9}{4} \qquad t_{11} = (1-\cos\tilde{\alpha})^{-1/2} \qquad t_{12} = (\cos\tilde{\alpha})^{-2} \qquad t_{13} = \left(1+t_{10}^2\right)^{-1} \tag{50}$$

$$t_{15} = t_{12}\,t_{13}\,\cos\alpha \qquad t_{16} = \lambda_v\,r^3 \qquad t_{17} = t_{11}\,t_{12}\,t_{13}\,\cos\alpha \qquad t_{18} = t_9\tan(\tilde{\alpha})^3$$

$$\frac{\partial \dot{\mathbf{r}}}{\partial \boldsymbol{\lambda}_v} = \frac{\partial \mathbf{a}_n}{\partial \boldsymbol{\lambda}_v} = \mu\beta\left(2\frac{\mathbf{r}^T\mathbf{n}}{r^4}\mathbf{n}\mathbf{r}^T + \frac{(\mathbf{r}^T\mathbf{n})^2}{r^4}\mathbf{I}_{3x3}\right)\frac{\partial \mathbf{n}}{\partial \boldsymbol{\lambda}_v} \tag{51}$$

$$\frac{\partial \mathbf{n}}{\partial \boldsymbol{\lambda}_v} = -\frac{\sin(\alpha)}{\sin(\tilde{\alpha})}\left(\frac{\mathbf{I}_{3x3}}{\lambda_v} - \frac{\boldsymbol{\lambda}_v\boldsymbol{\lambda}_v^T}{\lambda_v^3}\right) + \hat{\mathbf{i}}_r\left(\frac{\frac{\partial(\sin(\alpha+\tilde{\alpha}))}{\partial \boldsymbol{\lambda}_v}\sin\tilde{\alpha} - \frac{\partial(\sin\tilde{\alpha})}{\partial \boldsymbol{\lambda}_v}\sin(\alpha+\tilde{\alpha})}{\sin(\tilde{\alpha})^2}\right) \tag{52}$$

$$+\hat{\boldsymbol{\lambda}}_v \left(\frac{\frac{\partial(\sin\alpha)}{\partial \boldsymbol{\lambda}_v}\sin\tilde{\alpha} - \frac{\partial(\sin\tilde{\alpha})}{\partial \boldsymbol{\lambda}_v}\sin\alpha}{\sin(\tilde{\alpha})^2} \right)$$

where

$$\frac{\partial(\sin(\alpha+\tilde{\alpha}))}{\partial \boldsymbol{\lambda}_v} = \frac{\partial(\sin\alpha)}{\partial \boldsymbol{\lambda}_v}\cos\tilde{\alpha} + \sin\alpha\left(-\frac{\sin\tilde{\alpha}}{\cos\tilde{\alpha}}\right)\frac{\partial(\sin\tilde{\alpha})}{\partial \boldsymbol{\lambda}_v} + \sin\tilde{\alpha}\left(-\frac{\sin\alpha}{\cos\alpha}\right)\frac{\partial(\sin\alpha)}{\partial \boldsymbol{\lambda}_v} + \cos\alpha\,\frac{\partial(\sin\tilde{\alpha})}{\partial \boldsymbol{\lambda}_v} \tag{53}$$

$$\frac{\partial(\sin\tilde{\alpha})}{\partial \boldsymbol{\lambda}_v} = \frac{\cos\tilde{\alpha}}{\sin\tilde{\alpha}}\left(\frac{\mathbf{r}^T\boldsymbol{\lambda}_v}{r\lambda_v^3}\boldsymbol{\lambda}_v - \frac{\mathbf{r}}{\lambda_v r}\right) \tag{54}$$

$$\frac{\partial(\sin\alpha)}{\partial \boldsymbol{\lambda}_v} = -\left(\frac{12\,t_0\,t_{11}\,t_{15}}{16\,t_{16}\,t_8}\boldsymbol{\lambda}_v - \frac{3\,t_{17}}{4\,t_8\,t_3}\mathbf{r} + \frac{9\,t_0\,t_{11}\,t_{15}}{4\,t_{16}\,t_{18}}\boldsymbol{\lambda}_v - \frac{9\,t_{17}}{4\,t_{18}\,t_3}\mathbf{r}\right) \tag{55}$$

where all the coefficients are the ones defined in 50 except from $t_{16} = \lambda_v^3\, r$.

$$\begin{aligned}\frac{\partial \dot{\boldsymbol{\lambda}}_r}{\partial \mathbf{r}} = &-2\beta\mu\left[\frac{\mathbf{n}^T\boldsymbol{\lambda}_v}{r^3}\mathbf{a}\left(-\frac{\sin\alpha}{\cos\alpha}\,\frac{\partial(\sin\alpha)}{\partial\mathbf{r}}\right)^T - \frac{3}{r^5}\cos\alpha\,\mathbf{n}^T\,\boldsymbol{\lambda}_v\,\mathbf{a}\,\mathbf{r}^T + \frac{\cos\alpha}{r^3}\mathbf{a}\,\boldsymbol{\lambda}_v^T\,\frac{\partial\mathbf{n}}{\partial\mathbf{r}}\right.\\ &\left. + \frac{\cos\alpha}{r^3}\left(\mathbf{n}^T\boldsymbol{\lambda}_v\right)\left(\frac{\partial\mathbf{n}}{\partial\mathbf{r}} - \frac{2}{r^2}\left(r\left(\cos\alpha\,\mathbf{I}_{3x3} + \mathbf{r}\left(-\frac{\sin\alpha}{\cos\alpha}\,\frac{\partial(\sin\alpha)}{\partial\mathbf{r}}\right)^T\right) - \frac{\cos\alpha}{r}\mathbf{r}\mathbf{r}^T\right)\right)\right]\end{aligned} \tag{56}$$

where

$$\mathbf{a} = \mathbf{n} - 2\frac{\mathbf{r}^T\mathbf{n}}{r^2}\mathbf{r} \tag{57}$$

$$\begin{aligned}\frac{\partial \dot{\boldsymbol{\lambda}}_r}{\partial \boldsymbol{\lambda}_v} = -2\beta\mu\left[\frac{\mathbf{n}^T\boldsymbol{\lambda}_v}{r^3}\,\mathbf{a}\,\left(-\frac{\sin\alpha}{\cos\alpha}\,\frac{\partial(\sin\alpha)}{\partial\boldsymbol{\lambda}_v}\right)^T + \frac{\cos\alpha}{r^3}\mathbf{a}\,\boldsymbol{\lambda}_v^T\,\frac{\partial\mathbf{n}}{\partial\boldsymbol{\lambda}_v} + \frac{\cos\alpha}{r^3}\,\mathbf{a}\,\mathbf{n}^T\right.\\ \left. + \frac{\cos\alpha}{r^3}\left(\mathbf{n}^T\boldsymbol{\lambda}_v\right)\left(\frac{\partial\mathbf{n}}{\partial\boldsymbol{\lambda}_v} - \frac{2}{r}\mathbf{r}\left(-\frac{\sin\alpha}{\cos\alpha}\,\frac{\partial(\sin\alpha)}{\partial\mathbf{r}}\right)^T\right)\right]\end{aligned} \tag{58}$$

B. Computation of Jacobian matrix for rendezvous problem

In this Section of the Appendix the Jacobian matrix for a mission in which a rendezvous is performed at a NEA is detailed. This matrix:

$$\mathcal{J} = [\mathcal{J}_{\lambda_{r_0}} \ \mathcal{J}_{\lambda_{v_0}} \ \mathcal{J}_{t_f}]$$

Details of the various non-explicit derivatives are provided in Appendix VI.A.

$$\begin{bmatrix} \mathcal{J}_{\lambda_{r0}} & \mathcal{J}_{\lambda_{v0}} \end{bmatrix} = \begin{bmatrix} -\Phi_{\mathbf{r}\boldsymbol{\lambda}_r} & -\Phi_{\mathbf{r}\boldsymbol{\lambda}_v} \\ -\Phi_{\mathbf{v}\boldsymbol{\lambda}_r} & -\Phi_{\mathbf{r}\boldsymbol{\lambda}_v} \\ \mathbf{v}_0^T - \dot{\boldsymbol{\Psi}}^T(t_f) \begin{bmatrix} \Phi_{\lambda_r\lambda_r} \\ \Phi_{\lambda_v\lambda_r} \end{bmatrix} & -\frac{\mu \mathbf{r}_0^T}{r^3} + \mathbf{a}_n^T(t_0) + \frac{\partial \mathbf{a}_n}{\partial \boldsymbol{\lambda}_v}(t_0) - \dot{\boldsymbol{\Psi}}^T(t_f) \begin{bmatrix} \Phi_{\lambda_r\lambda_r} \\ \Phi_{\lambda_v\lambda_v} \end{bmatrix} \end{bmatrix} \tag{59a}$$

$$\mathcal{J}_{t_f} = \begin{bmatrix} \mathbf{v}_a - \mathbf{v}(t_f) \\ -\frac{\mu}{r_a^3}\mathbf{r}_a - \left(-\frac{\mu}{r(t_f)^3}\mathbf{r}^T(t_f) + \mathbf{a}_n(t_f)\right) \\ -\begin{bmatrix} \boldsymbol{\lambda}_r(t_f) \\ \boldsymbol{\lambda}_v(t_f) \end{bmatrix} \cdot \begin{bmatrix} -\frac{\mu}{r_a^3}\mathbf{r}_a \\ 3\frac{\mu}{r_a^5}\mathbf{r}_a\mathbf{v}_a \cdot \mathbf{r}_a - \frac{\mu}{r_a^3}\mathbf{v}_a \end{bmatrix} - \dot{\boldsymbol{\Psi}}(t_f) \cdot \begin{bmatrix} \dot{\boldsymbol{\lambda}}_r(t_f) \\ -\boldsymbol{\lambda}_r(t_f) \end{bmatrix} \end{bmatrix} \tag{59b}$$

C. Computation of Jacobian matrix for rendezvous problem with intermediate flyby

In this Section of the Appendix, it is analytically developed the Jacobian matrix for a mission in which a first flyby operation followed by a final rendezvous are performed at two different NEAs. This matrix:

$$\mathcal{J} = [\mathcal{J}_{\lambda_{r_0}} \ \mathcal{J}_{\lambda_{v_0}} \ \mathcal{J}_{\boldsymbol{\pi}} \ \mathcal{J}_{t_1} \ \mathcal{J}_{t_f}]$$

Details of the various non-explicit derivatives are provided in Appendix VI.A.

$$\mathcal{J}_{\lambda_{r0}} = \begin{bmatrix} -\Phi_{\mathbf{r}\lambda_r}(t_0, t_1) \\ \Phi_{\mathbf{r}\lambda_r}(t_0, t_f) \\ -\Phi_{\mathbf{v}\lambda_r}(t_0, t_f) \\ -2\boldsymbol{\pi}^T \Phi_{\mathbf{v}\lambda_r}(t_1, t_f) \\ \mathbf{f}^T(t_f)\Phi_{\lambda\lambda_r}(t_0, t_f) + \boldsymbol{\lambda}^T \begin{bmatrix} \Phi_{\mathbf{v}\lambda_r}(t_0, t_f) \\ \frac{\partial \mathbf{v}}{\partial \mathbf{r}}(t_f)\Phi_{\mathbf{r}\lambda_r}(t_0, t_f) + \frac{\partial \mathbf{v}}{\partial \lambda_v}(t_f)\Phi_{\lambda_v\lambda_r}(t_0, t_f) \end{bmatrix} \end{bmatrix} \tag{60a}$$

$$\mathcal{J}_{\lambda_{v0}} = \begin{bmatrix} -\Phi_{\mathbf{r}\lambda_v}(t_0, t_1) \\ -\Phi_{\mathbf{r}\lambda_v}(t_0, t_f) \\ -\Phi_{\mathbf{r}\lambda_v}(t_0, t_f) \\ -2\boldsymbol{\pi}^T \Phi_{\mathbf{v}\lambda_v}(t_1, t_f) \\ \mathbf{f}^T(t_f)\Phi_{\lambda\lambda_v}(t_0, t_f) + \boldsymbol{\lambda}^T \begin{bmatrix} \Phi_{\mathbf{v}\lambda_v}(t_0, t_f) \\ \frac{\partial \mathbf{v}}{\partial \mathbf{r}}(t_f)\Phi_{\mathbf{r}\lambda_v}(t_0, t_f) + \frac{\partial \mathbf{v}}{\partial \lambda_v}(t_f)\Phi_{\lambda_v\lambda_v}(t_0, t_f) \end{bmatrix} \end{bmatrix} \tag{60b}$$

$$\mathcal{J}_{\boldsymbol{\pi}} = \begin{bmatrix} \mathbf{0}_{3x3} \\ -\Phi_{\mathbf{r}\lambda_r}(t_1, t_f) \\ -\Phi_{\mathbf{r}\lambda_r}(t_1, t_f) \\ -\mathbf{v}^T(t_1) + (\mathbf{v}_{fb} - \mathbf{v}(t_1))^T \\ \mathbf{f}^T(t_f)\Phi_{\lambda\lambda_r}(t_1, t_f) + \boldsymbol{\lambda}^T \begin{bmatrix} \Phi_{\mathbf{v}\lambda_r}(t_1, t_f) \\ \frac{\partial \mathbf{v}}{\partial \mathbf{r}}(t_f)\Phi_{\mathbf{r}\lambda_r}(t_1, t_f) + \frac{\partial \mathbf{v}}{\partial \lambda_v}(t_f)\Phi_{\lambda_v\lambda_r}(t_1, t_f) \end{bmatrix} \end{bmatrix} \tag{60c}$$

$$\mathcal{J}_{t_1} = \begin{bmatrix} \mathbf{v}_{fb} - \mathbf{v}(t_1) \\ -\Phi_{\mathbf{r}\lambda_v}(t_1, t_f)\boldsymbol{\pi} \\ -\Phi_{\mathbf{v}\lambda_v}(t_1, t_f)\boldsymbol{\pi} \\ -\boldsymbol{\pi}^T\dot{\mathbf{v}}(t_1) + \boldsymbol{\pi}^T(\dot{\mathbf{v}}_{fb} - \dot{\mathbf{v}}) \\ (\Phi_{\lambda\lambda_v}(t_1, t_f)\boldsymbol{\pi})\mathbf{f}(t_1) + \boldsymbol{\lambda}^T(t_f)^T \begin{bmatrix} \Phi_{\mathbf{v}\lambda_v}(t_1, t_f)\boldsymbol{\pi} \\ \\ \frac{\partial \mathbf{v}}{\partial \mathbf{r}}(t_f)\Phi_{\mathbf{r}\lambda_v}(t_1, t_f)\boldsymbol{\pi} + \frac{\partial \mathbf{v}}{\partial \lambda_v}(t_f)\Phi_{\lambda_v\lambda_r}(t_1, t_f)\boldsymbol{\pi} \end{bmatrix} \end{bmatrix} \tag{60d}$$

$$\mathcal{J}_{t_f} = \begin{bmatrix} \mathbf{0}_{3x1} \\ \mathbf{v}_a - \mathbf{v}(t_f) \\ \dot{\mathbf{v}}_a - \dot{\mathbf{v}}(t_f) \\ 0 \\ \begin{bmatrix} \dot{\boldsymbol{\lambda}}_r(t_f) \\ \dot{\boldsymbol{\lambda}}_v(t_f) \end{bmatrix}^T \mathbf{f}(t_f) + \begin{bmatrix} \boldsymbol{\lambda}_r(t_f) \\ \boldsymbol{\lambda}_v(t_f) \end{bmatrix}^T \begin{bmatrix} \dot{\mathbf{v}}(t_f) \\ \frac{\partial \mathbf{v}}{\partial \mathbf{r}}(t_f)\dot{\mathbf{r}}(t_f) + \frac{\partial \mathbf{v}}{\partial \lambda_v}(t_f)\dot{\boldsymbol{\lambda}}_v(t_f) \end{bmatrix} - \boldsymbol{\lambda}(t_f) \cdot \ddot{\boldsymbol{\Psi}}(t_f) - \dot{\boldsymbol{\lambda}}(t_f) \cdot \dot{\boldsymbol{\Psi}}(t_f) \end{bmatrix} \tag{60e}$$

References

[1] Topputo, F., Wang, Y., Giordano, C., Franzese, V., Goldberg, H., Perez-Lissi, F., and Walker, R., "Envelop of reachable asteroids by M-ARGO CubeSat," *Advances in Space Research*, Vol. 67, 2021, pp. 4193–4221. https://doi.org/10.1016/j.asr.2021.02.031.

[2] Karatekin, Ö., Le Bras, E., Van wal, S., Herique, A., Tortora, P., Ritter, B., Scoubeau, M., and Manuel Moreno, V., "Juventas Cubesat for the HERA mission," European Planetary Science Congress, 2021. https://doi.org/10.5194/epsc2021-750.

[3] Dotto, E., Della Corte, V., Amoroso, M., Bertini, I., Brucato, J., Capannolo, A., Cotugno, B., Cremonese, G., Di Tana, V., Gai, I., Ieva, S., Impresario, G., Ivanovski, S., Lavagna, M., Lucchetti, A., Mazzotta Epifani, E., Meneghin, A., Miglioretti, F., Modenini, D., Pajola, M., Palumbo, P., Perna, D., Pirrotta, S., Poggiali, G., Rossi, A., Simioni, E., Simonetti, S., Tortora, P., Zannoni, M., Zanotti, G., Zinzi, A., Cheng, A., Rivkin, A., Adams, E., Reynolds, E., and Fretz, K., "LICIACube - The Light Italian Cubesat for Imaging of Asteroids In support of the NASA DART mission towards asteroid (65803) Didymos," *Planetary and Space Science*, Vol. 199, 2021, p. 105185. https://doi.org/10.1016/j.pss.2021.105185.

[4] Pugliatti, M., Piccolo, F., Rizza, A., Franzese, V., and Topputo, F., "The vision-based guidance, navigation, and control system of Hera's Milani CubeSat," *Acta Astronautica*, Vol. 210, 2023, pp. 14–28. https://doi.org/10.1016/j.actaastro.2023.04.047.

[5] Walker, R., Binns, D., Bramanti, C., Casasco, M., Concari, P., Izzo, D., Feili, D., Fernandez, P., Fernandez, J., Hager, P.,

Koschny, D., Pesquita, V., Wallace, N., Carnelli, I., Khan, M., Scoubeau, M., and Taubert, D., "Deep-space CubeSats: Thinking inside the box," *Astronomy & Geophysics*, Vol. 59, 2018, pp. 5.24–5.30. https://doi.org/10.1093/astrogeo/aty232.

[6] Oguri, K., and Lantoine, G., "Indirect trajectory optimization via solar sailing primer vector theory: Minimum solar-angle transfers," *Acta Astronautica*, Vol. 211, 2023, pp. 405–415. https://doi.org/10.1016/j.actaastro.2023.06.032.

[7] Johnson, L., "Solar sail propulsion for interplanetary small spacecraft," Space Propulsion 2018 (AIAA Seville 2018), 2018. URL https://ntrs.nasa.gov/citations/20180003091.

[8] McInnes, C. R., "Solar Sailing Technology, Dynamics and Mission Applications," Springer, London, 1999, Chap. 2, pp. 32–55.

[9] Mori, O., Shirasawa, Y., Mimasu, Y., Tsuda, Y., Sawada, H., Saiki, T., Yamamoto, T., Yonekura, K., Hoshino, H., Kawaguchi, J., and Funase, R., *Overview of IKAROS Mission*, Springer Berlin Heidelberg, Berlin, Heidelberg, 2014, pp. 25–43. https://doi.org/10.1007/978-3-642-34907-2_3.

[10] Biddy, C., and Svitek, T., "LightSail-1 solar sail design and qualification," *Proceedings of the 41st Aerospace Mechanisms Symposium*, 2012, pp. 451–463.

[11] Spencer, D. A., Betts, B., Bellardo, J. M., Diaz, A., Plante, B., and Mansell, J. R., "The LightSail 2 solar sailing technology demonstration," *Advances in Space Research*, Vol. 67, No. 9, 2021, pp. 2878–2889. https://doi.org/10.1016/j.asr.2020.06.029.

[12] Lappas, V., Pellegrino, S., Guenat, H., Straubel, M., Steyn, H., Kostopoulos, V., Sarris, E., Takinalp, O., Wokes, S., and Bonnema, A., "DEORBITSAIL: De-orbiting of satellites using solar sails," *2011 2nd International Conference on Space Technology*, 2011, pp. 1–3. https://doi.org/10.1109/ICSpT.2011.6064667.

[13] Lappas, V., Adeli, N., Visagie, L., Fernandez, J., Theodorou, T., Steyn, W., and Perren, M., "CubeSail: A low cost CubeSat based solar sail demonstration mission," *Advances in Space Research*, Vol. 48, 2011, p. 1890–1901. https://doi.org/10.1016/j.asr.2011.05.033.

[14] Barnes, N. C., Derbes, W. C., Player, C. J., and Diedrich, B. L., *Sunjammer: A Solar Sail Demonstration*, Springer Berlin Heidelberg, Berlin, Heidelberg, 2014, pp. 115–126. https://doi.org/10.1007/978-3-642-34907-2_8.

[15] Underwood, C., Viquerat, A., Schenk, M., Taylor, B., Massimiani, C., Duke, R., Stewart, B., Fellowes, S., Bridges, C., Aglietti, G., Sanders, B., Masutti, D., and Denis, A., "InflateSail de-orbit flight demonstration results and follow-on drag-sail applications," *Acta Astronautica*, Vol. 162, 2019, pp. 344–358. https://doi.org/10.1016/j.actaastro.2019.05.054.

[16] Tsuda, Y., Mori, O., Funase, R., Sawada, H., Yamamoto, T., Saiki, T., Endo, T., Yonekura, K., Hoshino, H., and Kawaguchi, J., "Achievement of IKAROS — Japanese deep space solar sail demonstration mission," *Acta Astronautica*, Vol. 82, No. 2, 2013, pp. 183–188. https://doi.org/10.1016/j.actaastro.2012.03.032, 7th IAA Symposium on Realistic Advanced Scientific Space MissionsAosta, Italy, July 2011.

[17] Zhao, P., Wu, C., and Li, Y., "Design and application of solar sailing: A review on key technologies," *Chinese Journal of Aeronautics*, Vol. 36, 2023, pp. 125–144. https://doi.org/10.1016/j.cja.2022.11.002.

[18] Lockett, T., Castillo-Rogez, J., Johnson, L., Matus, J., Lightholder, J., Marinan, A., and Few, A., "Near-Earth Asteroid Scout Flight Mission," *IEEE Aerospace and Electronic Systems Magazine*, Vol. 35, 2020, pp. 20–29. https://doi.org/10.1109/MAES.2019.2958729.

[19] Pezent, J. B., Sood, R., Heaton, A., Miller, K., and Johnson, L., "Preliminary trajectory design for NASA's Solar Cruiser: A technology demonstration mission," *Acta Astronautica*, Vol. 183, 2021, pp. 134–140. https://doi.org/10.1016/j.actaastro.2021.03.006.

[20] Okada, T., Kebukawa, Y., Aoki, J., Matsumoto, J., Yano, H., Iwata, T., Mori, O., Bibring, J.-P., Ulamec, S., and Jaumann, R., "Science Exploration and Instrumentation of the OKEANOS Mission to a Jupiter Trojan Asteroid using the solar power sail," *Planetary and Space Science*, Vol. 161, 2018, pp. 99–106. https://doi.org/10.1016/j.pss.2018.06.020.

[21] Rios-Reyes, L., and Scheeres, D., "Generalized Model for Solar Sails," *Journal of Spacecraft and Rockets*, Vol. 42, 2005, pp. 182–185. https://doi.org/http://hdl.handle.net/2027.42/76315.

[22] Gong, S.-P., Gao, Y.-F., and Li, J.-F., "Solar sail time-optimal interplanetary transfer trajectory design," *Research in Astronomy and Astrophysics*, Vol. 11, 2011, pp. 981–996. https://doi.org/10.1088/1674-4527/11/8/010.

[23] Heiligers, J., Fernandez, J. M., Stohlman, O. R., and Wilkie, W. K., "Trajectory design for a solar-sail mission to asteroid 2016 HO3," *Astrodynamics*, Vol. 3, 2019, pp. 231–246. https://doi.org/10.1007/s42064-019-0061-1.

[24] Saiki, T., Tsuda, Y., Funase, R., Mimasu, Y., Shirasawa, Y., and Demonstration Team, I., "Attitude Operation Results of Solar Sail Demonstrator IKAROS," *Transactions of the Japan Society for Aeronautical and Space Sciences, Aerospace Technology Japan*, Vol. 10, 2012, pp. To__1–To_4_6. https://doi.org/10.2322/tastj.10.To_4_1.

[25] Mengali, G., and Quarta, A. A., "Optimal three-dimensional interplanetary rendezvous using nonideal solar sail," *Journal of Guidance, Control, and Dynamics*, Vol. 28, 2005, pp. 173–177. https://doi.org/10.2514/1.8325.

[26] Caruso, A., Niccolai, L., Quarta, A. A., and Mengali, G., "Effects of attitude constraints on solar sail optimal interplanetary trajectories," *Acta Astronautica*, Vol. 177, 2020, pp. 39–47. https://doi.org/10.1016/j.actaastro.2020.07.010.

[27] Oguri, K., and McMahon, J. W., "Solar radiation pressure-based orbit control with application to small-body landing," *Journal of Guidance, Control, and Dynamics*, Vol. 43, 2020, pp. 195–211. https://doi.org/10.2514/1.G004489.

[28] Oguri, K., Lantoine, G., and McMahon, J. W., "Solar sailing primer vector theory: Indirect trajectory optimization with practical mission considerations," *Journal of Guidance, Control, and Dynamics*, Vol. 45, 2022, pp. 153–161. https://doi.org/10.2514/1.G006210.

[29] Peloni, A., Ceriotti, M., and Dachwald, B., "Solar-Sail Trajectory Design for a Multiple Near-Earth-Asteroid Rendezvous Mission," *Journal of Guidance, Control, and Dynamics*, Vol. 39, No. 12, 2016, pp. 2712–2724. https://doi.org/10.2514/1.G000470.

[30] Song, Y., and Gong, S. p., "Solar sail trajectory optimization of multi-asteroid rendezvous mission," *Acta Astronautica*, Vol. 157, 2018, pp. 111–122. https://doi.org/10.1016/j.actaastro.2018.12.016.

[31] Song, Y., and Gong, S., "Solar-Sail Deep Space Trajectory Optimization Using Successive Convex Programming," *Astrophys Space Sc*, Vol. 364, 2019, pp. 1–12. https://doi.org/10.1007/s10509-019-3597-x.

[32] Bailer-Jones, C. A. L., "The sun diver: Combining solar sails with the Oberth effect," *American Journal of Physics*, Vol. 89, No. 3, 2021, p. 235–243. https://doi.org/10.1119/10.0002178.

[33] He, J., Gong, S. P., Jiang, F. H., and Li, J. F., "Time-optimal rendezvous transfer trajectory for restricted cone-angle range solar sails," *Acta Mechanica Sinica/Lixue Xuebao*, Vol. 30, 2014, pp. 628–635. https://doi.org/10.1007/s10409-014-0033-x.

[34] Whittaker, E. T., and Robinson, G., "Lagrange's Formula of Interpolation, 17 in The Calculus of Observations: A Treatise on Numerical Mathematics," 4th ed. New York, 1967, pp. 28–30.

[35] Bryson, A. E., and Ho, Y. C., "Applied Optimal Control," Blaisdell, New York, 1969, Chap. 3.

[36] Jiang, F., Baoyin, H., and Li, J., "Practical techniques for low-thrust trajectory optimization with homotopic approach," *Journal of Guidance, Control, and Dynamics*, Vol. 35, 2012, pp. 245–258. https://doi.org/10.2514/1.52476.

[37] Bellman, R., Pontryagin, L. S., Boltyanskii, V. G. B., Gamkrelidze, R. V., and Mischenko, E. F., "Mathematical Theory of Optimal Processes," 1962, Chap. 1. URL https://api.semanticscholar.org/CorpusID:118166571.

[38] Zhang, C., Topputo, F., Bernelli-Zazzera, F., and Zhao, Y. S., "Low-thrust minimum-fuel optimization in the circular restricted three-body problem," *Journal of Guidance, Control, and Dynamics*, Vol. 38, 2015, pp. 1501–1509. https://doi.org/10.2514/1.G001080.

[39] Russell, R. P., "Primer vector theory applied to global low-thrust trade studies," *Journal of Guidance, Control, and Dynamics*, Vol. 30, 2007, pp. 460–472. https://doi.org/10.2514/1.22984.

[40] Taheri, E., Li, N. I., and Kolmanovsky, I., "Co-state initialization for the minimum-time low-thrust trajectory optimization," *Advances in Space Research*, Vol. 59, 2017, pp. 2360–2373. https://doi.org/10.1016/j.asr.2017.02.010.

[41] Hui, Y., and Hongxin, W., "Initial adjoint-variable guess technique and its application in optimal orbital transfer," *Journal of Guidance, Control, and Dynamics*, Vol. 22, 1999, pp. 490–492. https://doi.org/10.2514/2.7631.

[42] Wang, Y., Topputo, F., and Hou, X., "Analytic Gradients in Normalized Low-Thrust Trajectory Optimization with Interior-Point Constraints," *Journal of Guidance, Control, and Dynamics*, Vol. 47, 2024, pp. 1–11. https://doi.org/10.2514/1.G007896.